American Mineralogist, Volume 71, pages 406–427, 1986

Mineralogy and geochemical evolution of the Little Three pegmatite-aplite layered intrusive, Ramona, California

L. A. STERN,[1] G. E. BROWN, JR., D. K. BIRD, R. H. JAHNS[2]
Department of Geology, Stanford University, Stanford, California 94305
E. E. FOORD
Branch of Central Mineral Resources, U.S. Geological Survey, Denver, Colorado 80225
J. E. SHIGLEY
Research Department, Gemological Institute of America, 1660 Stewart Street, Santa Monica, California 90404
L. B. SPAULDING, JR.
P.O. Box 807, Ramona, California 92065

ABSTRACT

Several layered pegmatite-aplite intrusives exposed at the Little Three mine, Ramona, California, U.S.A., display closely associated fine-grained to giant-textured mineral assemblages which are believed to have co-evolved from a hydrous aluminosilicate residual melt with an exsolved supercritical vapor phase. The asymmetrically zoned intrusive known as the Little Three main dike consists of a basal sodic aplite with overlying quartz-albite-perthite pegmatite and quartz-perthite graphic pegmatite. Muscovite, spessartine, and schorl are subordinate but stable phases distributed through both the aplitic footwall and pegmatitic hanging wall. Although the bulk composition of the intrusive lies near the haplogranite minimum, centrally located pockets concentrate the rarer alkalis (Li, Rb, Cs) and metals (Mn, Nb, Ta, Bi, Ti) of the system, and commonly host a giant-textured suite of minerals including quartz, alkali feldspars, muscovite or F-rich lepidolite, moderately F-rich topaz, and Mn-rich elbaite. Less commonly, pockets contain apatite, microlite-uranmicrolite, and stibio-bismuto-columbite-tantalite. Several of the larger and more richly mineralized pockets of the intrusive, which yield particularly high concentrations of F, B, and Li within the pocket-mineral assemblages, display a marked internal mineral segregation and major alkali partitioning which is curiously inconsistent with the overall alkali partitioning of the system.

Calculations of phase relations between the major pegmatite-aplite mineral assemblages and supercritical aqueous fluid were made assuming equilibrium and closed-system behavior as a first-order model, although these assumptions may not be wholly correct. Isobaric phase diagrams were generated and are used to constrain the observed mineral assemblages in the system K_2O-Na_2O-Al_2O_3-SiO_2-H_2O as a function of temperature and cation-activity ratios of the coexisting fluid phase. Log activity-temperature plots of the stoichiometric assemblage microcline-albite-quartz-muscovite at 2 kbar show that $\log a_{(K^+/H^+)}$ of the fluid phase remains essentially constant throughout crystallization, while $\log a_{(Na^+/H^+)}$ rises slightly with falling temperatures. Modeling muscovite nonstoichiometry by decreasing activity of the pure component from unity to 0.5 markedly shifts the upper thermal stability limit of the assemblage microcline-albite-quartz-muscovite from approximately 630°C upward to 710°C. In the pegmatite-aplite system exposed at the Little Three main dike, crystallization temperatures are thought to have ranged from approximately 700°C downward toward 540°C at the central pocket zone; muscovite nonstoichiometry caused by F, Li, and Mn substitution may have contributed to the stability of this assemblage at the outer zones of the system, where stoichiometric muscovite is not predicted to be stable.

INTRODUCTION

The Little Three layered pegmatite-aplite intrusive, located in the Ramona pegmatite district of central San Diego County, California, is famous for its past production of gem-quality tourmaline and topaz, as well as for its yield of exceptional pocket matrix specimens. From a petrological viewpoint, this system presents an interesting example of a crystallization sequence of magmatic origin which is believed to have involved an initially water-

[1] Present address: U.S. Geological Survey, 345 Middlefield Road, Mail Stop 977, Menlo Park, California 94025.
[2] Deceased December 31, 1983.

0003–004X/86/0304–0406$02.00

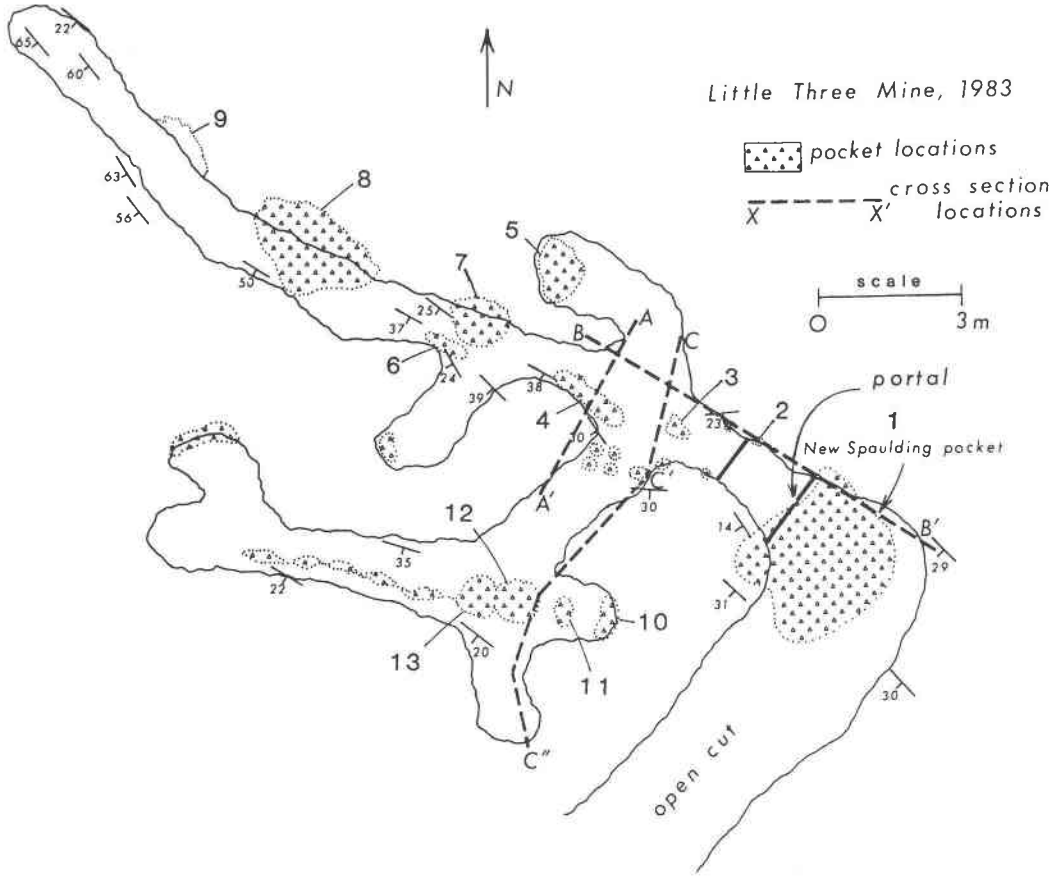

Fig. 1. Present workings of the Little Three mine.

saturated granitic residual fraction with exsolving and coexisting supercritical aqueous fluid (Jahns and Burnham, 1969). The Little Three main dike, exposed at the Little Three mine, exhibits a marked vertical contrast in texture, composition, and zoning patterns, such that massive and layered aplite defines the footwall of the intrusive, overlain by increasingly coarse-grained pegmatite and graphic pegmatite along the hanging wall. Centrally located "pockets" host a giant-textured suite of granitic mineral assemblages as well as some unusual accessory minerals.

This project was initiated over nine years ago when a large, richly mineralized pocket was discovered by L. B. Spaulding, Jr. A variety of museum-quality specimens were excavated from this exceptional pocket, and the structure and contents of the pocket were documented. A continuing collaboration between Spaulding and the Stanford workers also permitted documentation of the contents of other pockets within the main pegmatite dike, as well as of the zoning sequence of this asymmetrically layered body.

The internal zonation and three-dimensional nature of the Little Three main dike are explored in the present study, in conjunction with a detailed mineralogic study of the pocket material recovered from the mine since 1976, with emphasis on the large "New Spaulding" pocket. Equilibrium-phase-relation calculations are also presented here, serving as a first-order model to place some constraints on the fluid-solid interactions that took place during the evolution of this system. These calculations model the evolution of the pegmatite-aplite intrusive from coexisting silicate melt and supercritical aqueous fluid and are assessed through a series of isobaric phase diagrams relating calculated activity ratios of aqueous species and stable mineral assemblages in the system K_2O-Na_2O-Al_2O_3-SiO_2-H_2O. This graphical approach models general trends among cation-activity ratios and observed stable mineral assemblages, effected by changing temperature and mineral stoichiometry.

Location and general features

Numerous geologists have documented various features of the Ramona pegmatite district. The location of the San Diego County pegmatite districts is shown by Jahns and Wright (1951), and the general geological features of the Ramona district are described by Simpson (1965). General mineralogical and zonational features of San Diego County granitic pegmatites are described by Jahns (1955, 1982), Simpson (1962, 1965), Jahns and Tuttle (1963), Foord (1976, 1977), Shigley (1982), and Shigley and Brown (1985). Analyses of bulk composition and of average zone

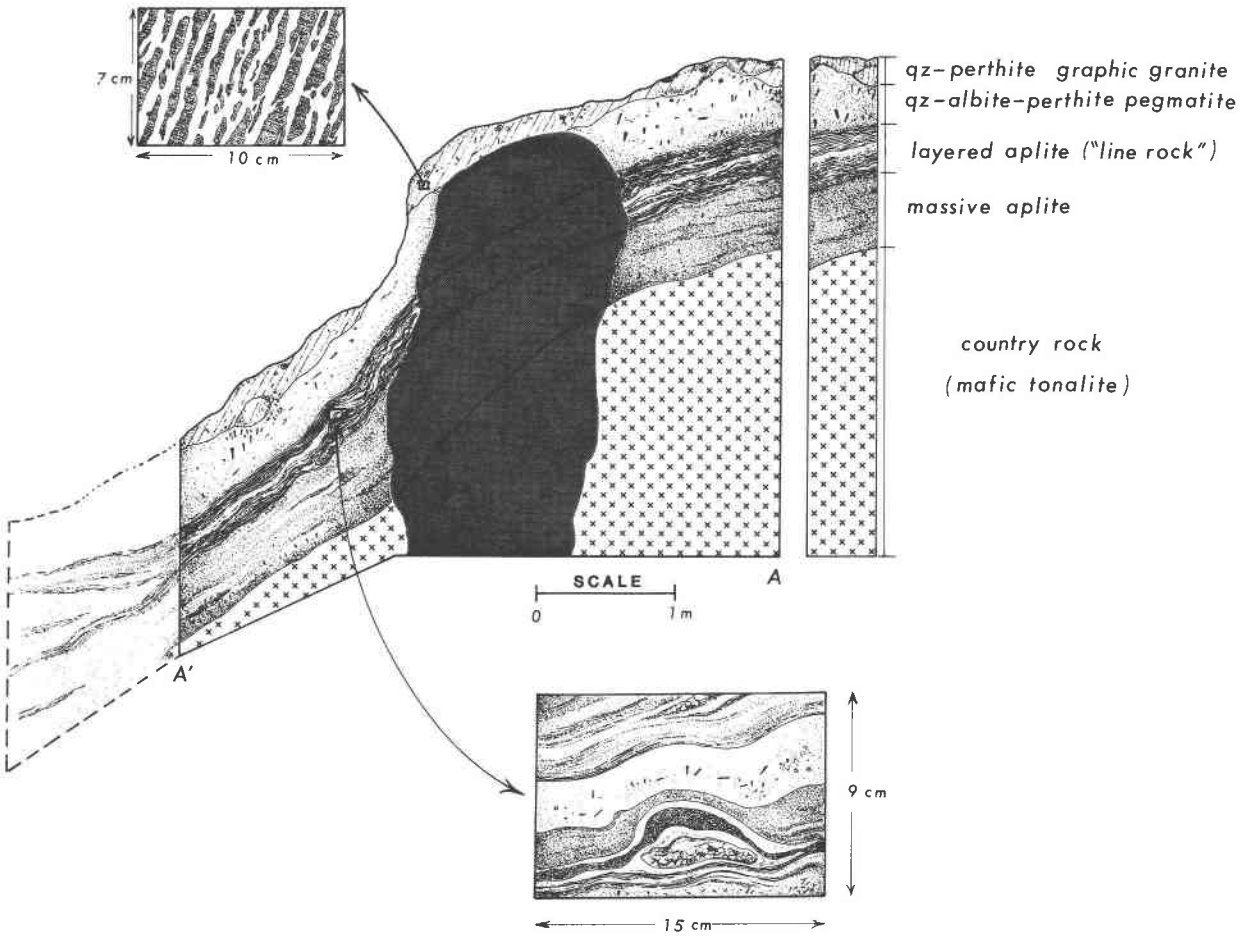

Fig. 2a. Cross section A–A′ across main tunnel (darkly shaded area), with vertical section showing units. Line rock locally splits and remerges down dip.

compositions of the Ramona district pegmatite-aplite intrusives are reported by Simpson (1965) and compared with layered pegmatite-aplite intrusives from other San Diego County localities by Jahns and Tuttle (1963). Fluid-inclusion and stable-isotope studies of San Diego County pocket pegmatite-aplite bodies are documented by Taylor et al. (1979).

The Little Three main dike is one of five principal pegmatite dikes on the Little Three property. These dikes, including the Little Three main dike, the Hercules-Spes-

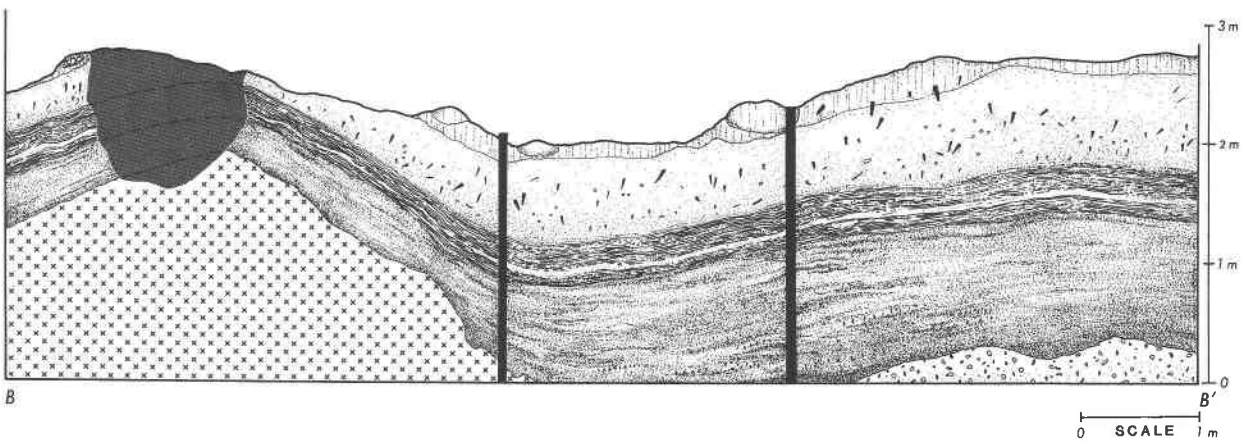

Fig. 2b. Cross section B–B′ along main tunnel. Darkly shaded area indicates small adit off of main tunnel.

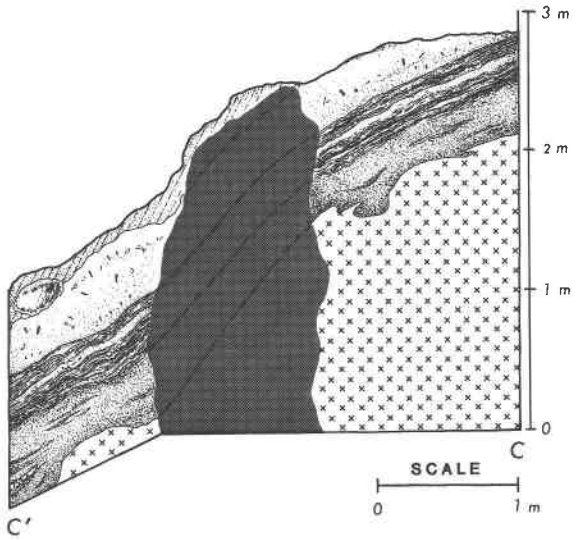

Fig. 2c. Cross section C–C′ across main tunnel (darkly shaded area).

sartine dike, the Spaulding dike, the Sinkankas dike, and the axinite-bearing Hatfield Creek dike, apparently formed as locally anastomosing but essentially separate intrusives. The Little Three dikes occur with other Ramona district and neighboring district pegmatite intrusives as a network of northwest-striking, southwest-dipping granitic dikes which principally intrude several gabbroic to tonalitic members of the Cretaceous Southern California batholith. A geologic map and cross-section through the central portion of the Ramona pegmatite district are given by Simpson (1965, Figs. 1 and 2).

The segment of the main dike exposed at the Little Three mine averages a N55°W strike, dipping 10°–65°SW, and transects a mafic facies of the Green Valley tonalite. The Little Three main dike crops out along hillside exposures where it is folded on a dip-slope orientation and runs perpendicular to it, presenting an irregularly rolling surface in cross-sectional view. A plan-view map of the present workings is shown in Figure 1, and the cross-sectional views of the layered intrusive illustrated in Figures 2a–2d show the rolling nature of the dike as well as the general concordancy of the internal zoning sequence. Locally the dike partially separates into two thinner, contiguous layering sequences, remerging down dip to a single thick sequence (Fig. 2a). The contact between the granitic pegmatite-aplite intrusive and the enclosing gabbroic-tonalitic wall rock is sharply defined, and the host rocks generally display little evidence of alteration except where proximal to large pockets.

Despite similar bulk compositions and asymmetrical zoning features among the dikes on the Little Three property, pocket-mineral assemblages vary significantly; each dike has its own characteristic pocket mineralogy, suggesting independent formation. While the Hercules-Spessartine "ledge" yields muscovite, microcline, albite, spessartine, schorl, quartz, plus minor Mn-rich axinite as

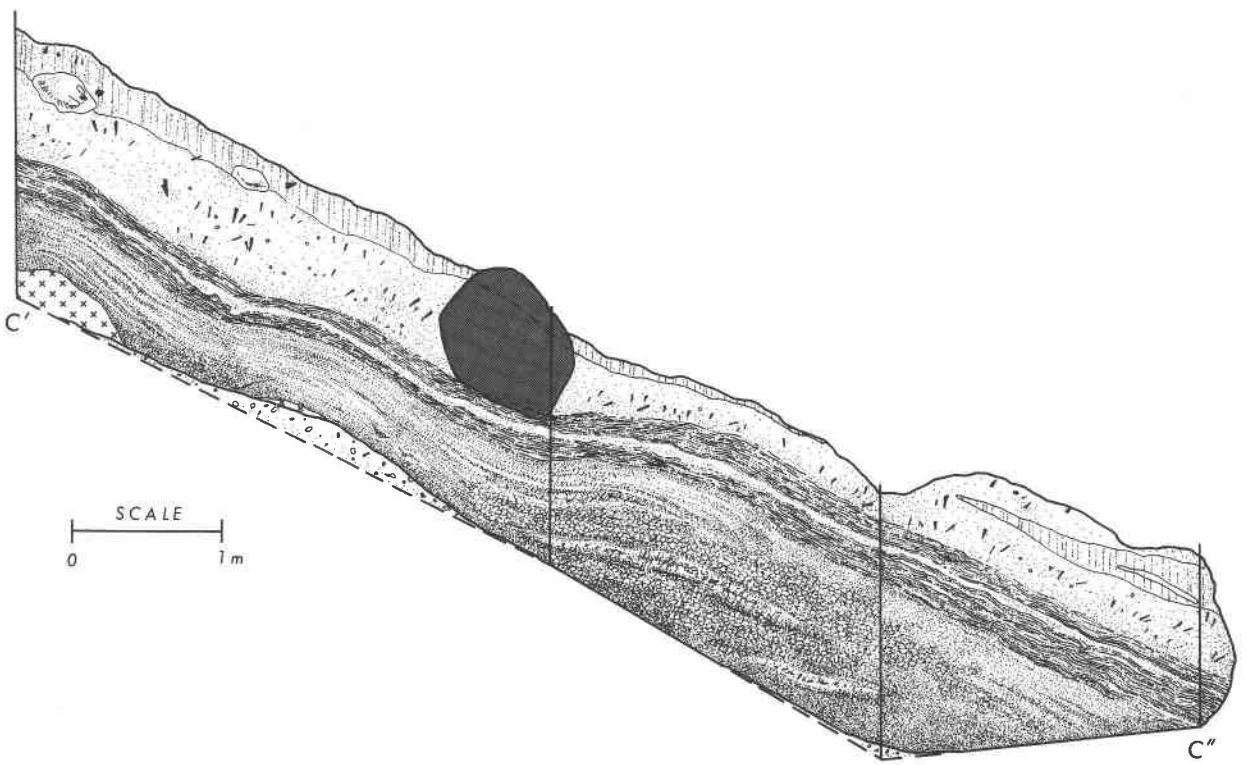

Fig. 2d. Cross section C′–C″ along adit dipping within plane of dike. Darkly shaded area indicates a smaller, secondary adit.

principal primary pocket minerals, pockets from the Little Three main dike have produced elbaite, muscovite or fluorine-rich lepidolite, quartz, microcline, albite, and topaz, plus minor apatite, microlite-uranmicrolite, stibiobismuto-columbite-tantalite, columbite, and native Bi. Several crystals of beryl and hambergite have also been extracted from the main Little Three workings. The Sinkankas dike has produced abundant hambergite, which has not been noted in the other dikes except for the few specimens recovered from the main dike. Yet another pegmatite dike on the property, the Hatfield Creek dike, produced abundant dark red-brown crystals of axinite.

Currently, the Little Three main dike is mined for tourmaline and topaz, and the adjacent Hercules-Spessartine ledge for spessartine and schorl. While a limited amount of mining has been done on the lower, southwestward extension of the main dike, the upper portions have proved far more productive. The most significant find was the New Spaulding pocket, occupying an area of approximately 2.2 m^3, from which many exceptional specimens were removed.

Internal zonation

Similar to layered pegmatite-aplite intrusives exposed in neighboring districts, the Little Three main dike displays a marked variation in texture, composition, and zoning patterns; while the aplitic footwall is rich in Na and relatively depleted in K, the coarse-grained overlying quartz-perthite-albite pegmatite and, particularly, the quartz-perthite "graphic granite" hanging wall are enriched in K while poorer in Na. A zone of cavities or pockets, partially lined or filled with euhedral crystals, is located within the upper-central section of the layered intrusive (Fig. 2a). Concentrating the minor and trace elements of the system, the pocket zone commonly hosts a giant-textured assemblage of major as well as minor phases of the system. Despite this vertical contrast, the minerals quartz + K-feldspar + albite plus subordinate muscovite + schorl + spessartine are stable in nearly all regions of the dike, and the bulk composition of the Little Three dike (Simpson, 1965) lies near the thermal low of the haplogranite system $KAlSi_3O_8$-$NaAlSi_3O_8$-SiO_2-H_2O (Jahns and Tuttle, 1963). The dike varies in thickness from approximately 1.4 to 2.1 m, and a vertical section is illustrated in Figure 2a.

Massive and layered aplitic footwall

Ranging from 0.5- to 1.0-m maximum thickness, the aplitic footwall comprises one-third to, locally, one-half of the zoned intrusive. The lower massive aplite varies in texture from a true fine-grained sugary appearance to lenses, pods, stringers, or particularly thick sections with coarser grain size. Albite and quartz are the predominant constituents of the aplite, with less abundant K-feldspar and schorl grains or needles. Muscovite and spessartine are only minor, sparsely distributed phases. Locally, the lowermost section of the aplite in contact with biotite tonalite wall rock may contain fine- to medium-grained biotite flakes. Biotite, however, rarely forms elsewhere in the intrusive.

The lower massive section grades upward compositionally to banded aplite or "line rock," ranging from 10- to 35-cm maximum composite thickness (Figs. 2b, 2d). The banded aplite consists of 0.1- to 4-cm-thick layers which alternate in appearance from white to dark gray, or less commonly, to orange brown. Varying concentrations of fine-grained schorl needles or spessartine grains sharply define thin, darker or varicolored laminations which are usually 1 to 4 mm thick. Neighboring lighter-colored bands that are poorer in tourmaline or spessartine tend to be thicker and coarser grained, with grain size ranging from 0.5 mm up to 4 cm. Coarse-grained lenses and pods locally interrupt the layering. These lenses are more potassic than the surrounding aplite laminations and may contain quartz, schorl, and potassic alkali feldspar megacrysts up to approximately 1.5 cm in length. Schorl needles are widely dispersed at all orientations throughout the aplite, but are most commonly oriented near-vertically, perpendicular to the hanging wall. While the layering of the line rock is roughly concordant with the attitude of the dike, small-scale fluctuations and undulations tend to form around coarse-grained pods and lenses, particularly those containing alkali feldspar megacrysts (Fig. 2a, inset).

Quartz-perthite-albite pegmatite

The contact above the banded aplite grades upward to increasingly coarse-grained, allotriomorphic, quartz-perthite-albite pegmatite. Schorl is subordinate but widespread throughout this zone, while muscovite aggregates and spessartine crystals are less abundant. Coarse-grained albite and intermediate microcline–hosted perthite make up the bulk of this zone, commonly altering to a sugary appearance on weathered surfaces. Large (up to 10 cm long), elongate, light-colored, intermediate microcline perthite crystals growing toward an adjacent pocket will often show an abrupt color change to darker appearance within several centimeters of the pocket; X-ray analyses indicate that this change in color immediately adjacent to a pocket is coincident with a symmetry inversion to the monoclinic state (Table 1). This change appears to take place within the single crystal, and the darker-colored orthoclase does not appear to form as a rind on the microcline perthite. The alkali feldspars enclose or are intergrown with anhedral quartz grains which vary in length from 0.3 cm upward to 2 cm. Schorl occurs as upwardly fanning rods frozen in the quartz-perthite-albite pegmatite. These crystals are commonly 0.3 to 2 cm in diameter and 0.8 to 5 cm in length, but proximal to the pocket zone they may reach 8 to 10 cm in length. Muscovite generally occurs in the pegmatite as sporadically distributed coarse-grained masses, more heavily concentrated near the pocket zone. Deep orange-brown to red-brown, idiomorphic spessartine crystals increase in abundance as well as in size toward the pocket line, ranging from 1 to 8 mm in diameter.

Quartz-perthite graphic granite

The predominant unit comprising the hanging wall of the Little Three dike is a quartz-perthite "graphic granite" (Fig. 2a, inset); perthite is the dominant constituent, consisting of a maximum microcline host with less-abundant, exsolved, low albite lamellae. The perthite encloses graphically oriented plates or rods of quartz arranged in parallel to subparallel fashion, which branch and reunite along the direction of elongation. The three-dimensional nature of the quartz-feldspar intergrowth has been documented by Simpson (1962).

The coarsely textured graphic granite hanging wall displays well-developed quartz and perthite crystal faces. The quartz-perthite ratio is approximately 1:3, and the microcline-albite ratio of the perthite is approximately 2.5:1 (Simpson, 1962). Schorl, spessartine, and muscovite are similarly distributed as they are in the underlying pegmatite, increasing in grain size and abundance toward the pocket line. The quartz-perthite intergrowth is often embayed or etched where it grows adjacent to a pocket.

Along the upper contact, a thin selvage of "border rock" separates the graphic granite from the country rock. This fine-grained selvage is composed chiefly of quartz, albite, and K-feldspar, plus less-abundant schorl needles and muscovite. Locally, the border zone contains appreciable amounts of biotite, although biotite is not encountered in the graphic granite immediately below. The upper border zone and graphic pegmatite hanging wall grade downward through a maximum thickness of 1 m to the giant-textured pocket zone and quartz-perthite-albite pegmatite below.

Table 1. Lattice parameters and X-ray data for pegmatite-zone feldspars

	intermediate microcline, from pegmatite-zone near pocket	orthoclase, adjacent to pocket	pocket orthoclase **
a (Å)	8.579(2)	8.556(2)	8.554(2)
b	12.967(2)	12.970(3)	12.965(2)
c	7.2125(1)	7.210(2)	7.2157(1)
α (°)	90.338(9)	90.	90.
β	115.970(8)	116.008(9)	116.031(9)
γ	89.121(6)	90.	90.
V (Å^3)	721.26	719.11	719.12
α*	90.063		
γ*	90.820		
#t_1o+t_1m (Al)	.92 ± .04	.90 ± .04	.95 ± .04
#t_1o-t_1m	.38 .04	0	0
##Z		.574	.636
##T (°C)		510 ± 20	430 ± 20
2θ° Cu Kα:			
$\bar{2}01$	21.01	21.02	21.03
130	22.42	23.56	23.56
060	41.76	41.76	41.76
$\bar{2}04$	50.59	50.62	50.65

* data for light-colored intermediate microcline (column 1) in quartz - K feldspar - albite pegmatite zone, and darker colored orthoclase (column 2) adjacent to pockets

** pocket orthoclase from claim immediately adjacent to Little Three

\# Al contents in ($t_1o + t_1m$) and ($t_1o - t_1m$) sites determined from b vs. c and α* vs. γ* plots given by Stewart and Wright (1974)

Z ordering parameter and corresponding freezing temperatures determined by b and c cell parameters, given by Hovis (1974) (Z = 7.6344 - 4.3584(b) + 6.8615(c))

The pocket zone

Although lenses and pods partially lined or filled with euhedral crystals are found in all zones of the layered intrusive, the true giant-textured pockets, miarolitic cavities, or small "bug holes" are chiefly confined along a pocket line which lies within the upper extent of the quartz-perthite-albite pegmatite zone, most commonly near or along the overlying graphic granite contact. The pocket line is always present, although it locally closes down to a thin selvage. Larger pockets commonly extend up into the graphic granite hanging wall, and the floor of such pockets may reach down into the layered aplite. While the smaller pockets or cavities are commonly ellipsoidal or ovoid, larger pockets are flatter and more irregularly oblate shaped, following the general attitude of the dike. Pockets may be either individually developed or interconnected by thin fissures or cracks. Locations of excavated pockets are shown in Figure 1, and brief descriptions of pocket contents are listed in Table 2. The pocket zone of the pegmatite concentrates minor elements of the system including F, Li, B, and Mn, as well as trace amounts of Nb, Ta, Rb, Cs, Ti, W, Sb, Bi, Sr, Ba, U, Ca, Ce, La, Pb, Sn, and Be. Larger pockets typically host giant-textured assemblages including quartz, maximum microcline megacrysts, coarsely bladed cleavelandite (low albite), Mn-rich elbaite, F-rich lepidolite or muscovite, and moderately F-rich topaz. Other pocket minerals that occur more rarely in the Little Three main dike include apatite, schorl, microlite-uranmicrolite, stibio-bismuto-columbite-tantalite, and columbite. Several specimens of pocket beryl (goshenite-morganite) and hambergite have also been recovered from the Little Three workings, as well as sparse amounts of pucherite. One pocket contained relicts of native Bi on the pocket floor surrounded by gray bismite and bismutite.

Of particular interest is the New Spaulding pocket, which was the largest pocket yet excavated from the Little Three, yielding many exceptional specimens and exhibiting strong mineral segregation and zonation. A reconstruction of this pocket is illustrated in Figure 3, and pocket contents are listed in Table 3. This very large pocket of approximately 2.2 m^3 was located at what is presently the entrance to the mine, occupying an irregularly shaped area within a zone 3.3 m × 3.3 m averaging 0.25 m in height. The attitude of the pocket was N45°W, 29°–31°SW, following a slight roll in the dike.

The contents of the New Spaulding pocket included quartz, tourmaline (elbaite), blue and colorless topaz, maximum microcline "pillars," clear and smoky quartz,

Table 2. Little Three main dike pocket descriptions

pocket #	description, and/or minerals in addition to quartz, cleavelandite, K feldspar
1	"New Spaulding pocket"; see Figure 4
2	Topaz, lepidolite, small dark-green tourmaline.
3	Small pocket located approximately 1' above layered aplite; contained tri-colored tourmaline "pencils", pink - light green - olive green.
4	Series of small, connected pockets along ceiling above main drift; contained irregularly shaped tourmaline coated with black (Mn?) oxide, smoky quartz, no topaz or lepidolite.
5	Connected by fractures to 4; contained black-brown smoky quartz, good matrix tourmaline and cleavelandite, several large olive-green tourmaline crystals, some shorl-capped. Pocket shorl only found here. Several "nail-head" tourmaline crystals found here. Coarse, abraded lepidolite.
6	Series of small tourmaline (dark green) pockets along ceiling above drift.
7	"Pasadena pocket"; uppermost extent of 6. Very little clay, essentially "dry". Light smoky green tourmaline pencils, topaz, floor covered with quartz. Blue apatite found down dip of Pasadena pocket.
8	Large pocket, 8' x 9' x 12-24", dipping approximately 45°. Floor-lining lepidolite, topaz found growing along floor at upper end of pocket and found loose at lower end; very large smoky quartz and K feldspar megacrysts located at upper end; several blue-green tourmaline pencils also found along upper extent of pocket. Also loose tourmaline pencils: gold-yellow bases with emerald-green caps.
9	Poor tourmaline.
10	Good topaz matrix specimens, much tourmaline, very little lepidolite.
11	Badly decomposed; some topaz, poor tourmaline.
12 - 13	Series of pockets along trough of large roll in dike; pockets of very large proportions, now collapsed. Topaz and tourmaline, mostly poorly shaped. 12: several quartz-topaz matrix specimens, poor tourmaline. Deep purple lepidolite frozen in and adjacent to pocket. Yellow pucherite here only.

* Pocket locations (column 1) refer to numbered pockets in Figure 1.

cleavelandite, fluorine-rich lepidolite, microlite-uranmicrolite, and stibio-bismuto-columbite-tantalite. Coarse-grained books of lepidolite irregularly lined the floor, with large megacrysts of maximum microcline resting on the floor and projecting upward with well-developed faces along the exposed surfaces (Fig. 3). Several smaller K-feldspar crystals were also removed from the roof of the pocket. Elbaite crystals were generally found attached to the roof within a mass of coarsely bladed cleavelandite. Only a small amount of cleavelandite (~20%) was found rooted to the floor of the pocket, and no lepidolite was attached to the roof, except for several lepidolite crystals attached to elbaite specimens. Large blue topaz crystals were removed from the wall of the pocket, and others were attached to both cleavelandite and lepidolite. A mass of intergrown topaz lined the back floor of the pocket, but was not obviously attached. Small colorless topaz crystals grew on the elbaite faces along the roof of the pocket. Abundant fragments of topaz were also removed from the pocket clay. Quartz crystals were less commonly found along the floor of the pocket than projecting down from the ceiling, and only those growing along the floor were coated with a fine-grained claylike mixture of K-feldspar plus muscovite and/or lepidolite. The majority of the stibio-bismuto-columbite-tantalite found in the pocket was attached to lepidolite and topaz along the floor of the pocket.

Virtually all of the pockets excavated from the Little Three mine were filled with wet, varicolored clays enclosing numerous fragments of primary pocket minerals as well as some organic matter (see Foord et al., 1986, for a description of pocket clays). The large pockets have all been found to contain surficial clays, but several pockets were found "dry." One such pocket was found immediately west of the New Spaulding pocket. This pocket contained only primary minerals with a fine white coating of K-feldspar and muscovite. Such pockets offer a view of pocket formation prior to low temperature and pressure surficial processes.

There has been sufficient fracturing of the dikes to allow entrance of surficial waters and organic material. Thin cracks are occasionally filled with flattened plant roots. Roots and organic material are particularly concentrated near pockets, due to the increased fracturing of the dikes in such areas. Within the New Spaulding pocket, numerous live, intertwining roots were removed from the clay contents.

Analytical methods

Chemical analyses of alkali feldspars, tourmaline, topaz, and lepidolite from the New Spaulding pocket, and of muscovite from the quartz-perthite-albite pegmatite zone, were obtained on a JEOL 733A electron microprobe using a beam current of 15 nA and an accelerating voltage of 15 kV. Each analysis represents a

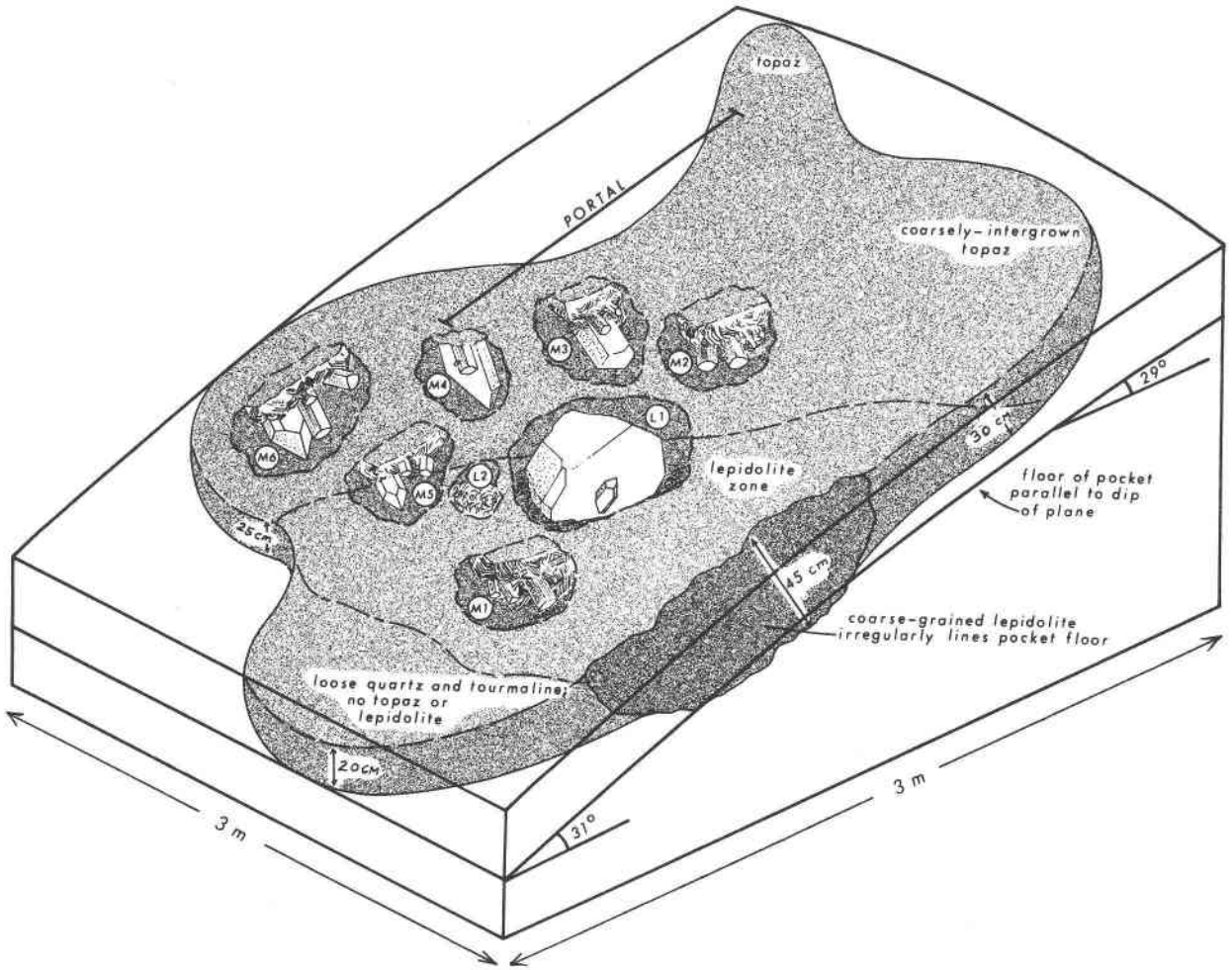

Fig. 3. Reconstruction of the New Spaulding pocket.

30-s counting interval or 0.3% standard deviation, with a beam diameter of 10 μm. Silicate mineral standards were used for analysis of Si, Al, K, Na, Ca, Mn, Mg, Fe, Ti, Sr, and Ba. A synthetic fluor-phlogopite standard was used for F analysis, and synthetic glass standards were used for Rb and Cs analysis. Data were corrected using the Bence and Albee (1968) procedure.

Chemical analyses of the stibio-bismuto-columbite-tantalite were obtained on a ARL EMX-SM electron microprobe using a beam current of 30 nA and an accelerating voltage of 15 kV, with a 5-μm beam diameter. Standards used were Si—quartz, Fe—Fe_2O_3, Nb—$BaSrNb_4O_{12}$, Ta—$MnTa_2O_6$, Bi—Bi_2O_3, W—$MnWO_4$, Ti—TiO_2, Sb—Sb_2O_3. Data were corrected using the program MAGIC IV (Colby, 1968).

The boron and lithium contents of pocket tourmaline were measured by inductively coupled plasma emission spectroscopy. Tourmaline samples were crushed to 200 mesh and dissolved in sodium carbonate.

Cell-dimension data were obtained by powder X-ray diffraction using an automated Rigaku DMAX powder diffractometer, Cu$K\alpha$ radiation, and operating conditions of 35 kV and 15 mA. Powdered samples were mixed to an approximate 5:1 ratio with an internal Si metal standard for precise calibration, and all samples were scanned with a 0.01° 2θ step width and 4.0-s counting period. Peak locations were determined with the aid of Rigaku peak-finding software. Least-square refinements of cell dimensions were calculated after the patterns were indexed with the aid of calculated patterns (Borg and Smith, 1969) for each mineral except lepidolite. Powder patterns for lepidolite were indexed on the basis of indexed patterns reported by Bailey (1980).

Pocket mineralogy

Quartz

Within the pocket zone, quartz may be clear, various smoky shades, or distinctly yellowish. Giant euhedral quartz crystals growing in large pockets tended to be rooted to the pocket ceiling, projecting downward to the center of the pocket, although smaller quartz crystals were also found rooted to the pocket floor. In smaller pockets, however, quartz was not preferentially situated in any specific area within the pocket. Solid inclusions within pocket quartz are minimal, but fluid inclusions are prevalent and often cast a milky appearance to the crystal. Several analyses of fluid inclusions from Little Three pocket quartz are given by Taylor et al. (1979).

Within the New Spaulding pocket and smaller pockets periph-

Table 3. Specimens recovered from the New Spaulding pocket

matrix specimen *	description
M1	3 large dark-green tourmaline crystals in cleavelandite matrix: (1) 4 x 5 x 6.5 cm long; (2) 3.5 x 4.5 x 3.5 cm long; (3) 3.5 x 2.0 x 3.5 cm long with small topaz crystals on the rims of 2. Medium-sized colorless quartz (12 x 12 x 15 mm). Lepidolite books on 2 of the tourmalines.
M2	2 large dark-green tourmaline crystals in cleavelandite matrix: (1) 6 x 5 x 7 cm long; (2) 4 x 5 x 6 cm with large quartz and K feldspar (20 x 15 x 10 cm).
M3	Large euhedral K feldspar crystal (9 x 10 x 14 cm) with some cleavelandite on sides. Also large dark-green tourmaline (4 x 5 x 7 cm), smaller dark-green tourmaline, and quartz.
M4	Very large smoky quartz (8 x 10 x 17.5 cm) with perfect termination; also large dark-green tourmaline (4.5 x 4.5 x 8 cm) with topaz on termination and on side.
M5	Large milky quartz crystal (6 x 7 x 9 cm); 2 large tourmaline crystals (4 x 5 x 6 cm, 4 x 3 x 3 cm); 1 colorless, euhedral topaz crystal (1 x 1.5 x 2 cm tall); set in cleavelandite matrix.
M6	3 large, dark-green tourmalines set in cleavelandite matrix: (1) 4.5 x 5.5 x 10 cm tall, with small, colorless topaz on rim; (2) 4.5 x 5 x 8 cm tall, with several topaz crystals on top and sides; (3) 5.5 x 5.5 x 6 cm, small colorless topaz on rim. Also large, smoky quartz crystal (5 x 10 x 14 cm) and small, colorless topaz.
L1	K feldspar (microcline) "pillar" (25 x 25 x 35 cm) resting on floor.
L2	Coarse books of lepidolite, irregularly lining floor.

* matrix specimens in column 1 refer to Figure 3

eral to it, excellent overgrowths on quartz substrates were observed, and fractured or broken pieces of quartz were commonly rehealed and overgrown. "Snow on the roof" texture is common on floor-attached quartz crystals, such that the substrate is covered with a fine white coating of K-feldspar plus muscovite and/or lepidolite, and in turn is dusted or covered by quartz. On several crystals, a multiple-stage growth history is shown, producing agatelike banding. The overgrowth is present on all faces of the quartz crystals, but is particularly developed on those faces first covered by the white K-feldspar plus mica coating. On some crystals which have developed overgrowths on completely clear substrates, color differences reveal multiple-stage growth.

Potassium feldspar

Like quartz, potassium feldspar is ubiquitous throughout all zones of the layered intrusive. Within the pocket zone, potassium feldspar commonly grows as large, single-phase, maximum microcline perthite megacrysts, ranging in color from light buff tan through darker shades of tan brown. Pocket feldspar crystals are euhedral and predominantly exhibit prism and pinacoid faces. Within the New Spaulding pocket, upward-growing megacrysts of approximately 30 cm × 30 cm × 25 cm appear to have served as "pillars" helping to prevent collapse of the pocket. Randomly oriented blades of cleavelandite are occasionally present within the K-feldspar blocks. The material from the New Spaulding pocket rarely, but on occasion, displays visibly developed overgrowths. A peculiarly rough, sawtoothlike surface is commonly exhibited on the feldspar surfaces. Where two crystals grow together, this serrated appearance is not present. The rough surfaces may be original primary growth features; some jagged sawtooth faces have the fine-grained white "snow on the roof" covering, thereby antedating the late-stage stagnant deposition of K-feldspar and muscovite.

Microprobe analyses, X-ray diffraction data, and cell-dimension calculations of the maximum microcline structure are listed in Table 4. Microprobe analyses of pocket microcline yield an average composition of $Or_{98}Ab_2$ and do not indicate any apparent zoning features. Minor amounts of Sr are preferentially incorporated into the microcline structure relative to the albite structure, but the microcline is essentially pure $KAlSi_3O_8$. Al/Si distribution between the T_1O and T_1m sites was determined from plots given by Stewart and Wright (1974) relating b and c cell edges and α^* and γ^* reciprocal lattice parameters; nearly complete ordering is indicated (Table 4). X-ray diffraction analysis of maximum microcline–hosted perthite from the graphic granite hanging wall are also listed in Table 4 for comparison.

Adjacent to the pocket zone, light-colored intermediate microcline–hosted perthite from the quartz-perthite-albite zone commonly shifts abruptly to a darker-colored orthoclase. Cell parameters determined from powder X-ray diffraction analyses of these feldspars are given in Table 1. Glassy pocket orthoclase collected from an exposure adjacent to the Little Three mine was analyzed and is also listed in Table 1.

Albite

Pocket albite occurs primarily as the coarsely bladed cleavelandite variety and less abundantly as lathlike inclusions within tourmaline or as exsolved lamellae within maximum microcline perthitic crystals. Pocket cleavelandite is commonly quite coarse grained, with individual bladed crystals ranging up to 2 cm across, 0.5 cm thick. The plates are clear to milky white, with no discernible overgrowth. Cleavelandite in the New Spaulding pocket grew abundantly along the ceiling and on some of the tourmaline crystals rooted to the ceiling. Cleavelandite was noticeably less abundant, however, along the floor of the pocket. In smaller pockets, cleavelandite was not preferentially located.

Table 4. Chemical and mineral data for maximum microcline

microprobe analyses			
	wt. % oxide*	formula proportions	
SiO_2	64.42	IV Si	3.00
Al_2O_3	18.07	VI Al	.99
FeO, Fe_2O_3	.08	Fe	< .01
CaO	.01		
Na_2O	.25	A Na	.02
K_2O	16.39	K	.98
SrO	.69	Sr	.02
BaO	.01		1.02
Total	99.92		

average composition: $(K_{.98}Na_{.02}Sr_{.02})(Al_{.99}Si_3O_8)$

Cell proportions		
	pocket specimen**	graphic granite#
a (Å)	8.5715(1)	8.555(2)
b	12.965(2)	12.964(4)
c	7.2198(1)	7.215(2)
α (°)	90.597(6)	90.616(9)
β	115.874(7)	115 85(1)
γ	87.705(6)	87.69(1)
V (Å^3)	721.33	721.13
α*	90.450	90.437
γ*	92.261	92.276
## t_1o+t_1m	.98 ± .04	.96 ± .04
## t_1o-t_1m	.99 ± .04	.99 ± .04
2θ° Cu Kα:		
$\bar{2}01$	21.04	21.04
131-1$\bar{3}$1	-.80	-.78
$\bar{2}04$	50.53	50.57

* average of 31 analyses from pocket megacryst (New Spaulding pocket)

** latice parameters for pocket megacryst

\# latice parameters for maximum microcline from graphic granite zone

Al contents in ($t_1o + t_1m$) and ($t_1o - t_1m$) sites determined from b vs. c and α* vs. γ* plots given by Stewart and Wright (1974)

Table 5. Chemical and mineral data for low albite

microprobe analyses			
	cleavelandite*	albite lamellae in perthite**	formula proportions*
SiO_2	68.22	68.55	IV Si 3.00
Al_2O_3	19.52	19.32	VI Al 1.01
FeO, Fe_2O_3	.09	.06	Fe < .01
CaO	.05	.01	
Na_2O	11.82	11.64	A Na .99
K_2O	.18	.15	K .01
BaO	.01	.01	1.00
SrO	.02	.06	
Total	99.91	99.80	

average cleavelandite composition: $(Na_{.99}K_{.01})AlSi_3O_8$

Cell proportions#			
a (Å)	8.1388(6)	α (°)	94.308(4)
b	12.7883(9)	β	116.581(4)
c	7.1576(6)	γ	87.660(3)
		α*	86.352
##Z	.78	γ*	90.464
##T (°C)	430 ± 20	### t_1o+t_1m (Al)	.97 ± .04
V (Å^3)	664.33	### t_1o-t_1m	.98 ± .04

* average of 25 analyses of cleavelandite from New Spaulding pocket

** average of 17 analyses of albite lamellae in maximum microcline perthite megacryst from New Spaulding pocket

\# latice parameters for pocket cleavelandite

Z ordering parameter based on b and c parameters (Z = -12.523 - 3.4065(b) + 7.9454(c)) and corresponding freezing temperature, given by Hovis (1974)

Al contents in ($t_1o + t_1m$) and ($t_1o - t_1m$) sites determined from b vs. c and α* vs. γ* plots given by Stewart and Wright (1974)

Microprobe analyses of pocket albite listed in Table 5 show slight differences between albite in the cleavelandite habit and albite inclusions in tourmaline or pocket microcline. Similar to the microcline analyses, the pocket albite is nearly pure in composition (Ab_{99}) and includes only trace amounts of Sr or Ba. Al/Si ordering based on cell dimensions (Table 5) shows that pocket albite can be classified as low albite.

Micas

Muscovite and lepidolite are both present within the pocket portion of the Little Three main dike. Although the amount of muscovite in the aplitic footwall is quite small, substantial quantities of muscovite or lepidolite are present in the pocket zone. While muscovite is typically green colored in the nonpocket pegmatite portion of the dike, it is commonly colorless or very light pink in the pocket zone. Peripheral to the New Spaulding pocket, green-zoned pocket muscovite with colorless cores was found; a similar color zoning is recorded within pocket tourmaline.

Light to medium-dark lavender-colored lepidolite is confined to the pocket zone. Within the New Spaulding pocket and in immediately adjacent smaller pockets, lepidolite was the only mica to form. Coarsely intergrown flat books of lepidolite covered much of the floor of the New Spaulding pocket, but was absent from the roof. Lepidolite books in the New Spaulding pocket grew to a maximum of 10 cm in diameter and 2 cm thick and occasionally exhibited unusual multiple growth fronts defined by minute inclusions of stibio-bismuto-columbite-tantalite, as well as occasionally being coated by this mineral.

Color-zoned red-violet lepidolite from small pockets west of the New Spaulding pocket was of different habit than the medium-lavender lepidolite from the New Spaulding pocket. The red-violet lepidolite shows excellent bow-tie structures, rather than the simple flat books associated with the New Spaulding pocket. All the muscovite found was flat and terminated within the pocket.

Microprobe analyses of lepidolite from the New Spaulding pocket are listed in Table 6; the average composition is $(K_{0.91}Na_{0.03}Rb_{0.07}Cs_{0.01})(Li_{1.86}Al_{1.09}Mn_{0.11}Fe_{0.01})(Si_{3.67}Al_{0.33})O_{10}(F_{0.93}OH_{0.06})_2$. The polytype of the lepidolite is 1M, and lattice constants are also listed in Table 6. Pocket lepidolite has nearly complete F replacement for OH, and microprobe analyses reveal an unusually high Si content. Microprobe traverses along coarsely bladed lepidolite, from base to termination, showed slight increases in the Al, Ti, Mn, and Rb contents accompanied by systematic decreases in the Si, K, and Cs contents. The Li and H_2O contents given were calculated by difference and by charge balance.

Table 6. Chemical and mineral data for lepidolite

	microprobe analyses wt. % oxide*	base**	term.***	formula proportions*		
SiO_2	55.62	57.88	54.88	IV	Si	3.72
Al_2O_3	18.25	17.00	19.83		Al	.28
TiO_2	.04	.02	.07			4.00
FeO, Fe_2O_3	.19	.19	.19	VI	Al	1.16
					Li	1.47
MnO	2.03	1.55	2.53		Mn	.12
MgO	.01	.01	.01		Fe	.01
CaO	.01	.01	.01			2.76
Na_2O	.20	.10	.24	A	K	.92
K_2O	10.79	11.04	10.43		Na	.02
Rb_2O	1.57	1.48	1.80		Rb	.07
Cs_2O	.39	.45	.35		Cs	.01
						1.02
F	8.90	8.6-9.2	8.6-9.2		F	1.88
#Li_2O	5.45				OH	.13
#H_2O	.30					2.01
-F = O	-3.74					
Total:	100.00					

average composition*:

$(K_{.92}Na_{.02}Rb_{.07}Cs_{.01})(Al_{.58}Li_{.74}Mn_{.06})_2(Al_{.28}Si_{3.72}O_{10})(F_{.94}OH_{.06})_2$

Cell proportions

a (Å)	5.218(2)	α (°)	90.
b	8.999(3)	β	100.41(2)
c	10.086(4)	γ	90.
		V (Å^3)	465.79

* average of 46 analyses of lepidolite from the New Spaulding pocket, from both coarse-bladed crystals lining the floor and from inclusions in tourmaline

** average composition at base of coarse-bladed crystals, rooted to pocket floor

*** average composition of crystal terminations, extending towards center of pocket

\# by difference

Table 7. Chemical and mineral data for topaz

	microprobe analyses# wt. % oxide	formula proportions		
SiO_2	32.62	IV	Si	1.00
Al_2O_3	55.66	VI	Al	2.00
FeO, Fe_2O_3	.06		Fe	< .01
F	16.86		F	1.63
*H_2O	1.90		OH	.38
-F = O	-7.1			2.01
Total	100.00			

average composition: $Al_2SiO_4(F_{.81}OH_{.19})_2$

Cell proportions

a (Å)	4.6505(3)	α(°)	90.
b	8.7987(6)	β	90.
c	8.3879(6)	γ	90.
		V (Å^3)	343.184

\# Average of 61 analyses of topaz from the New Spaulding pocket. Analyses are from early-stage topaz inclusions in tourmaline, and from late stage topaz growing on tourmaline rims. No zoning or systematic chances noted.

* by difference

Topaz

Topaz is found only in the pocket portion of the Little Three main dike, occurring as two or more generations. Excellent topaz specimens were recovered from the New Spaulding pocket; in excess of 28 kg of topaz were removed in the form of approximately 75 nearly complete crystals. The earliest topaz crystals to form are commonly the largest, and are pale to medium blue or blue green. Fluid inclusions up to 1 mm in diameter are present in these larger topaz crystals. Early generation topaz also occurs as small inclusions within tourmaline. In the New Spaulding pocket, many of the larger blue topaz crystals were found loosely scattered along the floor, not obviously attached to either the floor or to the ceiling. Several blue topaz crystals were, however, observed to be attached to the wall of the pocket. Much smaller, colorless, flawless topaz crystals which grew only to a maximum of several millimeters in diameter, are found perched on most pocket minerals, particularly on the elbaite specimens. Growth spirals are well developed on the faces of topaz, as is the case with tourmaline and quartz. Gem-quality material is only found within the smaller topaz crystals; the early-formed blue crystals are virtually all microfractured.

Approximately 65 topaz crystals sampled primarily from the New Spaulding pocket, ranging in weight from 0.06 to 0.6 kg, were examined in order to characterize their general morphology. Two general types were distinguished, based on terminations. The first type is characterized by well-developed (001) basal-pinacoid terminations typical of Russian topaz from the Ural Mountains. These crystals were bound by large (110) and (120) prism faces, and about 50% of them had large (021) dome faces. The second type had roof-shaped terminations made up of intersecting (011) and/or (021) dome faces, bound by (110) and (120) prism faces. The generalized sequence of the most important faces in order of decreasing relative area is (110), (120), (011), (001), and (111). This sequence deviates somewhat from the predictions of Donnay-Harker (1937) theory, but is reasonably consistent with the theory that the best-developed faces have a high density of intraplane bonds.

In ultraviolet light, the basal sections of topaz from the New Spaulding pocket show fossil growth zones outlined by yellow fluorescence. One light-blue topaz crystal contained 0.03% Ge; the fluorescence may be caused by zonation of Ge, or perhaps by lines of fluid inclusions.

Microprobe analyses listed in Table 7 reveal a moderately high F content of pocket topaz, and yield an average composition of $Al_2SiO_4(F_{0.82}OH_{0.20})_2$. No significant differences or zonations were found between the various generations of topaz crystals analyzed. Lattice parameters for pocket topaz are also listed in Table 7.

Tourmaline

Pocket tourmaline from the dike exhibits a variety of forms. Although schorl is present within the aplite footwall of the dike as well as in the nonpocket pegmatite and graphic granite hanging wall, it has only been found in one pocket of the Little Three main dike (Table 2, no. 5). Elbaite is prevalent throughout the pockets, and the bulk of the material removed is of varying shades from dark green to yellow green, or more rarely, amber colored or pink. While some of the larger pockets contain giant dark-

green tourmaline crystals intergrown with a cleavelandite matrix along the roof of the pocket, many pockets have produced tourmaline "pencils" enclosed in pocket clay. In one pocket, "nailhead" tourmaline with sharply chiseled terminations was removed (Table 2, no. 5). Tourmaline pencils are commonly olive green or light smoky green, but tricolored pink to light-green to olive-green pencils also have been removed. One large pocket produced pencils with gold-amber–colored bases capped by emerald-green terminations (Table 2, no. 8). Doubly terminated crystals are not uncommon, and all intact pocket tourmaline specimens except for those with the nailhead terminations exhibit the simple basal (0001) termination.

Several exceptional matrix specimens were recovered from the New Spaulding pocket. Of all the attached tourmaline removed from this pocket, approximately 90% was rooted to the ceiling, projecting downward. Only about 10% of the crystals were rooted to the floor, and no tourmaline was encountered with lepidolite along the floor. Those tourmaline crystals that did project up from the floor were relatively small, rarely exceeding 2-cm maximum diameter, while those projecting downward occasionally exceeded 5 cm in diameter. Over 91 kg of tourmaline was extracted from the New Spaulding pocket, and conditions of the crystals ranged from excellent to poor. While some were badly fractured or incipiently altered, others were smooth and lustrous on the prism faces and nearly free of flaws. Approximately 30% of the crystals from the New Spaulding pocket were doubly terminated or showed significant addition of material on the broken surface. Much of the material within this pocket had been broken off from their original location of growth. When sectioned perpendicular to the **c** axis, concentric growth zoning is exhibited primarily toward the rim.

Virtually all the tourmaline crystals from the New Spaulding pocket and pockets immediately adjacent to it and up dip from it had the simple (0001) termination; however, one specimen which was sectioned normal to the **c** axis showed that at one point in the growth history the termination was more complex, with both (0001) and (1010) developed. Most of these crystals had the (1010) face grow itself out of existence, leaving only the (0001). Other crystals from other portions of the dike, however, appear to have had only the (0001) termination developed at all stages of growth.

Tourmaline crystals from the New Spaulding pocket or peripheral smaller pockets occasionally exhibited solid inclusions of microlite-uranmicrolite with radiation haloes around them; a red color was locally imparted on the host tourmaline, regardless of the initial color. The microlite-uranmicrolite was found only within the outermost zone material of the tourmaline. The final material to crystalize in this pocket and those around it was pink in color, presumably due to an increase in the Mn/Fe ratio. The late-stage pink material is particularly evident on broken crystals, as overgrowth and repaired fractures, and in the form of pencils.

Tourmaline from the New Spaulding pocket was sectioned normal to the **c** axis and microprobed for composition and for zoning trends. The analytical results are listed in Table 8, and the average composition is $Na_{0.8}(Al_{1.17}Li_{0.75}Mn_{0.83}Fe_{0.21})Al_6(Si_{5.95}O_{18})(B_{2.99}O_9)(F_{0.31}OH_{1.69})_2$. The sectioned samples vary in appearance from medium-green–amber cores to dark-green rims. Some concentric zoning is present within the samples, but the more prominent color change is to the dark-green rim material.

Although the pocket tourmaline from the Little Three main dike is correctly referred to as elbaite, the unusually high Mn content places the composition along a possible solid solution between pure endmember elbaite [where the X, Y, and Z cation sites are occupied by Na, (Al,Li), and Al] and the hypothetical endmember tsilaisite (where the X, Y, and Z sites are occupied by Na, Mn, and Al). Other high Mn–bearing tourmaline and the possible elbaite-"tsilaisite" solid solution are discussed by Kunitz (1929), Slivko (1959), Schmetzer and Bank (1984), and Dietrich (1985). The Fe content varies widely throughout the samples; although there was no systematic change noted from core to rim, local zones contain little or essentially no Fe. The Mn content is highest at the core, decreasing slightly toward the rim or termination. Although some Fe-depleted zones yielded slightly increased Mn contents, there was no strong correlation noted. B and Li contents were analyzed on six core, midrim, and termination samples by inductively coupled plasma techniques and showed no systematic changes associated with location in the crystal. The F content in the samples fluctuated, but showed a general, although marginal, increase toward the rim. The Na content was found to remain essentially constant, but is unusually low. Calculating the number of ions in the formula based on 31 (O,OH,F) indicates that while the Y and Z sites are full, the X site is only 80% full (Table 8).

Cell-dimension data for pocket-zone elbaite are given in Table 8. Cell parameters determined for schorl sampled from the quartz-perthite-albite pegmatite zone are also listed in Table 8 and are

Table 8. Chemical and mineral data for tourmaline

	microprobe analyses: average composition*	core**	rim**	formula proportions*		
SiO_2	36.60			Si	5.95	
TiO_2	.12			B	2.99	
Al_2O_3	37.42			Al	6.00	Z
FeO, Fe_2O_3	1.61					
MnO	6.05	6.85	5.60	Al	1.17	
MgO	.01			Mn	.83	Y
CaO	.03			Li	.75	
Na_2O	2.55			Fe	.21	
K_2O	.02				2.96	
F	1.18	.87	1.35	Na	.80	
#B_2O_3	10.65			K	<.01	X
#Li_2O	1.15			Ca	<.01	
##H_2O	3.12				.81	
				F	.61	
-F = O	-.50			OH	3.38	
					3.99	
Total	100.00					

average composition:

$$Na_{.80}(Al_{1.17}Li_{.75}Mn_{.83}Fe_{.21})Al_6(Si_{5.95}O_{18})(B_{2.99}O_9)(F_{.30}OH_{1.69})_2$$

Cell proportions	pocket elbaite	schorl, from pegmatite zone
a (Å)	15.913(6)	15.979(5)
b	15.913(6)	15.979(5)
c	7.138(3)	7.165(2)
α (°)	90.	90.
β	90.	90.
γ	120.	120.
V (Å^3)	1565.40	1584.42

* average of 90 analyses of green elbaite from the New Spaulding pocket

** systematic changes from core to rim of sample

\# B and Li analyzed by ICP methods

\#\# H_2O by difference

Table 9. Chemical data for stibio-bismuto-columbite-tantalite

	microprobe analyses wt. % oxide*	range	formula proportions*	
Sb_2O_3	37.23	28.73 - 44.93	Sb	0.84
Bi_2O_3	13.55	7.27 - 21.67	Bi	0.19
TiO_2	1.27	0.40 - 2.24	Ti	0.05
SiO_2	0.01	---	Si	---
Nb_2O_3	24.75	11.63 - 37.02	Nb	0.61
Ta_2O_5	19.44	5.93 - 27.96	Ta	0.29
WO_3	2.29	1.10 - 4.28	W	0.03
FeO	0.06	0.0 - 0.12	Fe	---
Total:	98.60			

average composition: $(Sb_{.84}Bi_{.19})(Nb_{.61}Ta_{.29}W_{.03})O_4$

*average of 15 analyses of stibio-bismuto-columbite-tantalite from the New Spaulding pocket

significantly larger than those calculated for pocket elbaite, as expected from compositional differences.

Apatite

No large crystals of apatite were found within the New Spaulding pocket, but one large crystal of K-feldspar was coated with tiny, colorless apatite, topaz, and stibio-bismuto-columbite-tantalite. Several clear blue and pink fragments were found in one pocket west of the New Spaulding; both varieties fluoresce yellow–yellow orange under SW UV light. No well-formed crystals were encountered, and the fragments are 1–2 cm in maximum diameter, with hopper faces.

Microlite-uranmicrolite

Specimens of this mineral series are rare and have not been found larger than approximately 1 mm in diameter, but the crystals are always euhedral and intact. Based on textural relations, this late-stage pocket mineral formed coevally with pink tourmaline, second-generation topaz, and stibio-bismuto-columbite-tantalite. Microprobe spectral scans of one grain included within a doubly terminated tourmaline crystal from a small pocket up dip and adjacent to the New Spaulding showed Ta, Nb (such that Ta > Nb), Ti, Bi, Ca, U, Na, and F to be major elements, and Mn, Ce, La, Pb, Sb, and Sn as minor elements in addition to O and H. Radiation damage is present around grains of uraniferous microlite.

Stibio-bismuto-columbite-tantalite

This late-stage pocket mineral is black in hand specimen, red brown in thin section, and forms as euhedral crystals ranging from less than 0.01 mm to 2 cm in length. An estimated 500 crystals weighing a total of approximately 1 kg were recovered from the New Spaulding pocket. Polysynthetic twinning is commonly present, and several specimens display irregular color boundaries. Complete details are given by Foord (1982a).

Compositions of this mineral were determined to be intermediate between stibiotantalite-stibiocolumbite and bismutotantalite-bismutocolumbite (not known naturally). Four markedly inhomogeneous crystals of stibio-bismuto-columbite-tantalite were analyzed (Foord, 1982a, 1982b) and yielded unique compositions with highly variable Sb, Bi, Nb, and Ta contents (Table 9). Of additional interest is the presence of W and Ti, which are uncommon for either bismutotantalite or stibiotantalite-stibiocolumbite. The calculated average structural formula for this mineral, on the basis of four oxygen atoms, is $(Sb_{0.84}Bi_{0.19})(Nb_{0.61}Ta_{0.29}W_{0.03})PO_4$.

Columbite

One, flattened, tabular crystal of columbite (1 cm × 3 cm × 0.75 cm) from a pocket in the main dike west of the New Spaulding pocket was analyzed by emission spectrography and found to contain major Nb and Mn, as well as 7% Fe, 0.3% Ti, 0.15% Zr, and 1.5% Ta.

K-feldspar + muscovite coating

Within the New Spaulding pocket, minerals and fragments that had fallen to the floor were covered with a veneer of white, hard, porcelanous coating resembling montmorillonite, but identified as fine-grained K-feldspar plus muscovite. Included within the coating, which may be as thick as 1 cm, are fragments of topaz, albite, and tourmaline, and the coating is commonly intercalated with fine-grained quartz.

Many of the primary pocket minerals within the New Spaulding pocket show some faces with this dusting or coating. The matrix pieces intact along the ceiling possessed the least, while the material at the bottom was completely coated except for where the coating had broken off. This "snow on the roof" coating appears to reflect nearly stagnant precipitation of the fine-grained assemblage. Pockets in other locations within the dike occasionally exhibit floor-rooted crystals that are coated preferentially on only half of the exposed faces, possibly indicating unidirectional flow within the late-stage pocket fluids.

Crystallization of the Little Three Main Dike

Despite the curious variation in texture, composition, and zoning patterns observed at the Little Three mine, the closely associated fine-grained to giant-textured mineral assemblages suggest common paragenetic evolution from a single system. The genetic model proposed by Jahns and Burnham (1969) for igneous granitic pegmatites credibly accounts for most features observed at the Little Three. The framework of their model postulates closed-system crystallization in the presence, successively, of a hydrous silicate melt, of melt and coexisting aqueous fluid, and finally of the supercritical fluid phase alone. This model, based upon experimental studies as well as on field observations of many layered pegmatite-aplite dikes, emphasizes the role of water both as a dissolved constituent in the granitic derivative magma and as the major component of the fluid phase. Formation of the San Diego pegmatite-aplite dikes from a magmatic origin with an exsolving aqueous-fluid phase is also supported by isotopic data presented by Taylor et al. (1979).

The apparently early-stage alkali partitioning observed at the Little Three dike strongly supports early vapor saturation and its subsequent separation as a medium through which K and other constituents are preferentially removed from the footwall melt and transported toward the hang-

ing wall. Experimental data reported by Jahns and Burnham (1969) indicate that in a water-saturated granitic system with coexisting supercritical aqueous fluid, K is removed from the melt by the vapor phase in preference over Na and can travel rapidly to the hanging wall via the vapor phase in response to a temperature gradient. With a starting composition near the thermal minimum for the confining pressure, loss of K plus other volatiles could result in the formation of the fine-grained sodic footwall primarily from residual melt, with K transferred to the crystallizing K-rich hanging wall by the volatile water-rich fraction. The composition of the giant-textured graphic granite does not correlate to either the minimum or to any cotectic of the $NaAlSi_3O_8$-$KAlSi_3O_8$-SiO_2-H_2O system as determined by Tuttle and Bowen (1958). Recent experimental studies of graphic granites by Fenn (1986) indicate that graphic intergrowths of quartz and K-feldspar are produced by *non*equilibrium crystallization in pegmatitic melts with water contents ranging from undersaturated to saturated. These textures were not produced in water-supersaturated runs, which instead produced separate idiomorphic crystals. This evidence suggests that the graphic granites present in the hanging wall of pegmatites like the Little Three main dike formed from a water-rich melt rather than primarily from a supercritical vapor phase (cf. Martin, 1982, vs. Simpson, 1962), with K enrichment enhanced by the presence of an exsolved vapor phase. Small cavities distributed throughout the hanging wall also support the presence of a fluid phase during the formation of the graphic pegmatite hanging wall.

Pocket material presumably formed in the near or virtual absence of silicate melt, after the melt had been largely exhausted by crystallization of the anhydrous solid phases predominant in the aplitic and pegmatitic portions of the dike. The rarer alkalis and metals of the system became sufficiently concentrated in these pocket subsystems to allow crystallization of minerals containing these elements as major constituents. Such minerals include fluorine-rich lepidolite, elbaite, topaz, microlite-uranmicrolite, stibiobismuto-columbite-tantalite, and columbite.

Pocket rupture is believed to occur when the internal pressure of the pocket exceeds the confining strength of the surrounding dike material. A certain overstepping of pressure is necessary to activate the rupture process; the continued build-up of the proportion of aqueous-vapor phase exsolved from the silicate melt, perhaps enhanced by the crystallization of tourmaline (London, 1986a), is believed to be the mechanism by which the internal pressure is increased. Depending on the geometry of the pocket and the rate of escape of contained fluid, the rupture event may be minor to catastrophic. In the case of the New Spaulding pocket, the available evidence suggests that rupture was violent, and pocket minerals were broken off and fractured extensively, producing doubly terminated crystals and repaired fragments of crystals. Subsequent rupture events and later through-flowing aqueous solutions resulted in additional breakage. Such material has no discernible overgrowths, however. The abrasion of pocket minerals and mineral fragments occurred during both pocket rupture and postrupture aqueous flow. The lepidolite on the floor of the New Spaulding pocket was rounded and abraded on the terminations which had no porcelainous coating on them. It appears that abrasion occurred after formation of the white coating, which in turn postdated pocket rupture.

Temperature constraints

Results of experiments conducted by Jahns and Burnham (1969) on the water-saturated haplogranite system indicate that crystallization of San Diego–type granitic pegmatites, following exhaustion of the silicate melt, can be expected to persist down to temperatures of approximately 600–550°C under confining pressures of approximately 2 kbar, where the presence of such components as HF, B_2O_3, and Li_2O suppresses the final crystallization temperature toward the lower limit given. Oxygen and deuterium isotopic data given by Taylor et al. (1979) on minerals, whole-rock samples, and fluid inclusions from pocket quartz from a suite of San Diego gem-bearing pegmatite-aplite dikes support the experimental temperature and pressure range determined by Jahns and Burnham, although lower temperatures for formation of tourmaline-bearing pockets are suggested by London (1986b). Taylor et al. (1979) concluded from their data that the intrusives were emplaced at temperatures of approximately 700–730°C, followed by supersolidus crystallization of the lower aplite and upper border zones persisting to temperatures down through approximately 540°C. Formation of the graphic granite hanging wall occurred over a temperature range of approximately 630–540°C (Taylor et al., 1979), indicating that graphic granite crystallization took place at lower temperatures than the aplitic footwall and did not crystallize until after a significant portion of the basal aplite had formed (Taylor et al., 1979; Foord, 1976; Jahns and Burnham, 1969). These temperature determinations are based in part on isotopic equilibration between hydrous minerals and a coexisting aqueous fluid with $\delta D = -50‰$, which is consistent with δD values obtained on fluid inclusions from Little Three pocket quartz reported by Taylor et al. (1979).

Subsolidus formation of the pocket zone is believed to have persisted over an average temperature range of 40–50°, from approximately 565 to 520°C, or lower, under a confining pressure of approximately 2 kbar, which may have increased as pocket formation progressed (Taylor et al., 1979). This pocket-crystallization temperature range is partly based on an average $\Delta^{18}O$ of 0.45‰ between base and termination of pocket quartz sampled from San Diego pegmatite-aplite dikes (Taylor et al., 1979). The data which they reported for quartz overgrowths on Little Three pocket quartz, however, yield a $\Delta^{18}O$ difference of 1.8‰ compared to core values, suggesting that either deposition of the overgrowths persisted through considerably lower temperatures than core formation, or that there was an abrupt increase in the isotopic composition of the fluid.

Equilibration of pocket minerals at lower temperatures is also supported by Z ordering parameters determined for albite and orthoclase found within or proximal to the New Spaulding pocket; Z values were calculated from equations given by Hovis (1974) and Thompson et al. (1974) relating *b* and *c* cell parameters to Al/Si ordering. The results of these calculations are listed in Tables 1 and 5 and yield temperatures from 500°C down toward 420°C. While these calculated temperatures are not presumed to be absolute, they do suggest equilibration to significantly lower temperatures than those for primary pocket crystallization.

Pocket evolution: Role of volatile constituents

Crystallization of phases in large pockets such as the New Spaulding pocket, with unusually high hyperfusible concentrations, was probably strongly influenced by the volatile constituents. The New Spaulding pocket, unlike smaller miarolitic cavities, displays strong mineral segregation; K-rich minerals such as fluorine-rich lepidolite and microcline crystals are preferentially distributed along the floor of the pocket, while Na- and B-bearing minerals such as cleavelandite and elbaite form the matrix lining the roof. This alkali segregation is the reverse of that observed throughout the bulk of the layered intrusive, where the basal section is sodic while the hanging wall is potassic. Most Mn is concentrated in elbaite, although Mn is also present in the floor-lining lepidolite. Most quartz crystals project down from the roof, suggesting that Si activity is also increased roofward. Fluorine-bearing minerals are distributed between both roof and floor, but floor-lining fluorine-rich lepidolite has nearly complete F for OH replacement while only partial replacement is found in elbaite. Topaz with moderately high F contents is ubiquitous. Li and Al distributions appear to be approximately uniform throughout the pocket.

The behavior of granitic melts with excess H_2O, as well as the range of crystallization and solidus temperatures of such systems, has been shown experimentally to vary considerably with F content (Wyllie and Tuttle, 1961; Bailey, 1977; Manning, 1981; Dingwell et al., 1985), B content (Chorlton and Martin, 1978; Pichavant, 1981, 1983), and Li content (Stewart, 1978; Burnham and Jahns, 1962; Wyllie and Tuttle, 1964). The high concentrations of F, B, and to a lesser extent Li, may be largely responsible for the internal zoning of large pockets such as the New Spaulding. That F activity dominates over Li activity at the Little Three is indicated by the abundance of F-bearing tourmaline in addition to high-F topaz and virtually F-end-member lepidolite. Li is present in the mica and tourmaline structure, but the common lithium aluminosilicates associated with Li-rich pegmatites, such as petalite, spodumene, and eucryptite (London and Burt, 1982), are noticeably absent from the Little Three. Lithium aluminosilicates have been observed to exhibit pseudomorphic replacement by albite and micas (London and Burt, 1982), and some lithium micas have been observed and experimentally shown to be secondary metasomatic products generated by the action of late F-bearing aqueous fluids on early lithium aluminosilicates and K-feldspars (Hawthorne and Černý, 1982; Stewart, 1978, 1963; Munoz, 1971). Pocket micas and feldspars from the Little Three show no evidence of replacing pre-existing minerals, however, and appear to be primary phases.

Experimental studies on the roles of F and B in water-saturated granitic melts reveal several important factors that may bear on pocket formation. Wyllie and Tuttle (1961) noted that the increase in F content in the system serves to depress liquidus temperatures, enhances crystallization from the vapor phase, and depolymerizes the melt into which F preferentially partitions relative to the vapor phase. Experimental data reported by Manning (1981) on the role of F on the water-saturated haplogranite system at 1 kbar concur with the findings of Wyllie and Tuttle (1961) and support the conclusion that F serves to increase the silicate solute content of the vapor phase. Manning also noted that increased F content in the melt displaces the quartz–K-feldspar–albite minimum liquidus position away from that for the F-free system and toward the albite apex.

Experimental data discussed by Pichavant (1981, 1983) on the role of B_2O_3 on the water-saturated granite system indicate that B serves as a network-forming cation, increasing the solubility of SiO_2 in the aqueous fluid, and strongly modifies the distribution of Na, K, Si, and Al between melt and vapor phases. While the vapor phase in the experiments was found to become enriched in B, Si, and Na, the melt was enriched with K and Al. The partition coefficient of B_2O_3 between silicate melt and a coexisting vapor phase was experimentally determined by Pichavant (1983) to be approximately 0.33 ± 0.02 at 1 kbar. While this partition coefficient favors the vapor phase, significant amounts of B_2O_3 are still able to dissolve in the silicate melt.

The implications of the experimental work with respect to pocket formation suggest that the F plus B contents of large pockets serve not only to depress liquidus temperatures, but also to strongly modify the distribution of the alkalis and to ultimately enhance crystallization from the vapor phase by increasing the silicate solute capability of the aqueous fluid. Assuming that some residual melt was present during pocket formation and was distributed floorward, then the experimentally determined effects of high B and F concentrations may account for the floorward distribution of K-rich minerals (lepidolite, K-feldspar), while Na-, B-, and Si-rich minerals (cleavelandite, elbaite, quartz) are preferentially distributed roofward in several of the larger pockets. Formation of the large pockets may have been largely influenced by the F-, B-, and Li-rich aqueous-vapor phase; crystallization occurred primarily from the volatile-rich vapor phase in the presence of nominal amounts of residual silicate melt, with subsequent crystallization from the vapor phase only, and persisted to considerably lower temperatures than the F-, B-, and Li-deficient pockets.

Phase-equilibria calculations and predictions

The geochemical evolution of the Little Three pegmatite-aplite dike during crystallization can be approximately modeled with phase-equilibria calculations relating the observed mineral assemblages and a supercritical aqueous fluid. These relations are evaluated in the present study through isobaric phase diagrams, which constrain phase boundaries as a function of temperature and activity ratios of aqueous-electrolyte species in the system Na_2O-K_2O-Al_2O_3-SiO_2-H_2O. The mineral assemblage K-feldspar + albite + quartz + muscovite is of primary interest here, owing to the stability of this assemblage throughout all zones of the system. A similar approach for modeling stable assemblages observed at the Spruce Pine pegmatite is discussed by McTigue (1981). Not only does this graphical approach allow relationships between stable mineral assemblages and calculated activity ratios of aqueous electrolytes to be assessed at crystallization temperatures, but this method also indicates the sensitivity of reactions to fluctuations in temperature, cation activity, and mineral stoichiometry. Because the bulk composition of the Little Three dike lies near the thermal minimum of the haplogranite system (Simpson, 1965; Jahns and Tuttle, 1963), this procedure provides a limiting-case example of the evolution of the composite pegmatite-aplite sequence; however, these phase-equilibria calculations model the water-rich granite system and are not meant to apply to the high F-, B-, and Li-bearing pocket subsystems. Similar modeling of such pockets is not currently possible owing to insufficient thermodynamic data for pocket minerals and aqueous species bearing F, B, and Li.

The system observed at the Little Three is assumed here to have maintained closed-system conditions, which is a reasonable assumption concluded by Taylor et al. (1979) from the isotopic disparity between San Diego pegmatite-aplite intrusives and the wall rocks into which they are emplaced. The calculations presented here assume no significant CO_2 present in the fluid phase, supported by fluid-inclusion data from Little Three pocket quartz given by Taylor et al. (1979), and assume unit activity of H_2O. The assumption of equilibrium in these calculations is not as well founded, and crystallization of certain portions of the dike system (e.g., graphic granite) may be best described as nonequilibrium; however, these approximations provide a reasonable model for the actual system and serve as a useful point of departure for initial calculations to illustrate general trends in the supercritical aqueous phase.

Thermodynamic data base

Prediction of equilibrium phase relations between a fluid phase and the observed pegmatite-aplite mineral assemblages requires calculations of equilibrium constants for only those reactions in the system Na_2O-K_2O-Al_2O_3-SiO_2-H_2O involving quartz. The presence of quartz in all assemblages observed in the Little Three main dike justifies the constraint of quartz saturation used here. The thermodynamic properties of reactions involving minerals and water, as well as aqueous species at temperatures less than 550°C, are computed by the Fortran program SUPCRT from equations, data, and coefficients given by Helgeson and Kirkham (1974, 1976), Walther and Helgeson (1977), and Helgeson et al. (1978, 1981). Thermodynamic properties of aqueous species at temperatures greater than 550°C at 2 kbar are computed from equations and data reported by Mckenzie (1980) and Mckenzie and Helgeson (1984). Thermodynamic data for fluor-topaz given by Barton et al. (1982) were also incorporated into the data base and are used in the calculations. The standard state adopted for minerals and liquid H_2O calls for unit activity of the pure substance at any pressure and temperature, and that for aqueous electrolytes corresponds to unit activity of a hypothetical one molal solution referenced to infinite dilution at any pressure and temperature.

Equilibrium phase relations

The addition of the aqueous-species data to the SUPCRT data base permits the pegmatite-aplite phase relations to be evaluated at the elevated temperatures of interest, at 2 kbar. This can be achieved most readily by plotting stable quartz-bearing assemblages as a function of temperature and logarithmic activity ratios of the electrolytes in solution. Reactions within the system $KAlSi_3O_8$-$NaAlSi_3O_8$-SiO_2-H_2O were balanced conserving Al^{3+}, thereby allowing the ratios of log $a_{(K^+/H^+)}$ and log $a_{(Na^+/H^+)}$ to be evaluated. Generating mass-action equations for reactions within the two subsystems permits the activity ratios log $a_{(K^+/H^+)}$ and log $a_{(Na^+/H^+)}$ to be solved for in terms of the equilibrium constants calculated by SUPCRT, as well as the activity of minerals if nonstoichiometric. Because the equilibrium constants for the isobaric reactions considered here are temperature dependent, the mass-action equation corresponding to a given reaction constrains stability field boundaries as a function of temperature, aqueous-electrolyte activity, and nonstoichiometric mineral or H_2O activity.

The graphs shown in Figures 4a and 4b plot the stable, stoichiometric mineral assemblages at quartz saturation from 30 to 900°C, at 2 kbar, for the two subsystems K_2O-Al_2O_3-SiO_2-H_2O and Na_2O-Al_2O_3-SiO_2-H_2O, respectively. Figure 4a shows that within the crystallization-temperature range 700–540°C, muscovite will not appear as a stable phase with K-feldspar and quartz until temperature falls below 630°C, with a corresponding log $a_{(K^+/H^+)}$ of approximately 4.00. Because

$$-\Delta H_r^\circ/RT^2 = (\partial \ln a_{(K^+/H^+)}/\partial T)_P \approx 0$$

for the K-feldspar–muscovite reaction at crystallization temperatures, log $a_{(K^+/H^+)}$ remains essentially constant as temperature falls toward 540°C, producing the nearly horizontal topology of the K-feldspar–muscovite boundary. The phase relations depicted in Figure 4a also suggest that formation of muscovite at 630°C takes place in response

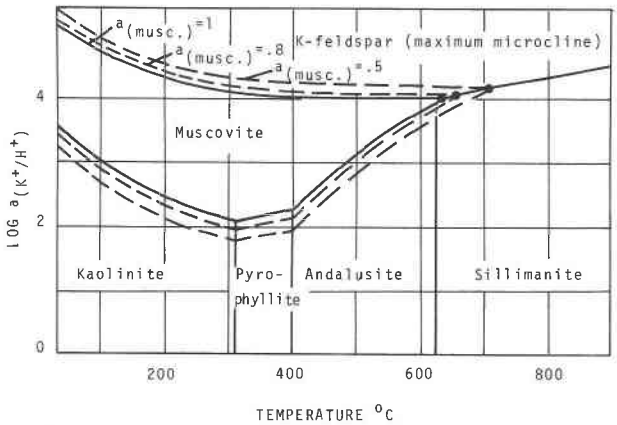

Fig. 4a. Phase relations for the system K_2O-Al_2O_3-SiO_2-H_2O plotted as a function of temperature and log $a_{(K+H+)}$, for pegmatite-aplite mineral assemblages in equilibrium with a supercritical aqueous fluid. $P_T = P_{H_2O}$ = 2 kbar; a_{H_2O} = 1. Solid lines denote stability field boundaries calculated for stoichiometric minerals at quartz saturation. Dashed lines contour decreasing $a_{KAl_2(AlSi_3)O_{10}(OH)_2}$. As activity of the pure muscovite component decreases from 1 down to 0.5, the upper thermal stability limit of the assemblage K-feldspar (maximum microcline) + muscovite + quartz increases from 640°C up to 710°C.

Table 10. Chemical data for muscovite

	microprobe analyses* wt. % oxide		formula proportions	
SiO_2	45.87	IV	Si	3.04
Al_2O_3	36.87		Al	.96
TiO_2	.07			4.00
FeO, Fe_2O_3	1.21	VI	Al	1.92
MnO	.08		Fe	.06
MgO	0.0		Ti	< .01
CaO	0.0		Mn	< .01
Na_2O	1.05			1.99
K_2O	10.28	A	Na	.14
F	.96		K	.86
#H_2O	4.00			1.00
-F = O	-.40		F	.20
			OH	1.77
Total	100.00			1.97

average composition:

$(K_{.86}Na_{.14})(Al_{.96}Fe_{.03}Ti_{.005}Mn_{.005})_2(Al_{.96}Si_{3.04}O_{10})(F_{.10}OH_{.88})_2$

* average of 12 analyses of non-pocket muscovite, from the pegmatite zone

\# H_2O by difference

to, and at the expense of, the breakdown of sillimanite. Yet the absence of both sillimanite or andalusite from all observed assemblages in the pegmatite-aplite dike, as well as the presence of muscovite at the outer zones of the system, indicates that stoichiometric mineral assemblages plotted in the temperature range 700–540°C are not consistent with the observed sequences.

The occurrence of muscovite in the upper hanging wall as well as in the lower aplite, where early-stage crystallization temperatures were presumably greater than 630°C, suggests that the likely source of inconsistency lies in the first approximation made concerning mineral stoichiometry. Because the K-feldspar–muscovite boundary rises only slightly with decreasing temperatures, minor substitutions into either the K-feldspar or muscovite structure produces a substantial shift in the upper thermal stability limit of the assemblage K-feldspar + muscovite + quartz. Figure 4a illustrates the significant expansion of the stability field for muscovite with increasing deviation from stoichiometry. As muscovite activity is reduced to 0.8, the upper thermal stability range is boosted from 630 to 655°C with the corresponding log $a_{(K^+/H^+)}$ ratio increasing from 4.00 to 4.05. Further reduction of the activity of the pure muscovite component to 0.5 expands the muscovite stability field to 710°C, with log $a_{(K^+/H^+)}$ of the coexisting fluid phase increasing to 4.2.

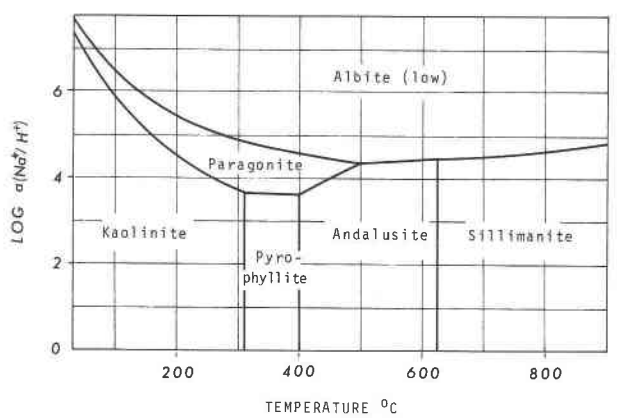

Fig. 4b. Phase relations for the system Na_2O-Al_2O_3-SiO_2-H_2 plotted as a function of temperature and log $a_{(Na+/H+)}$. $P_T = P_{H_2O}$ = 2 kbar; a_{H_2O} = 1. Solid lines show stability field boundaries calculated for stoichiometric minerals at quartz saturation.

Nonstoichiometric muscovite in the Little Three dike may account for the common occurrence of the assemblage K-feldspar + albite + muscovite + quartz in most regions of the pegmatite-aplite dike, including early-stage crystallization areas where stoichiometric muscovite is not predicted to be stable. Microprobe analyses of pocket feldspar and micas from the Little Three main dike show that pocket lepidolite contains nearly complete F substitution into the hydroxyl site, as well as significant Li substitution and Mn substitution for octahedral Al. Alkali feldspar analyses, however, yield nearly pure end-member compositions. These data suggest that the minor elements of the system are preferentially incorporated into the mica structure relative to the alkali feldspar structures, serving to significantly expand the muscovite stability field, and thereby stabilizing the assemblage K-feldspar + albite + muscovite + quartz at outer zones of the system where the stoichiometric assemblage is not predicted to be stable.

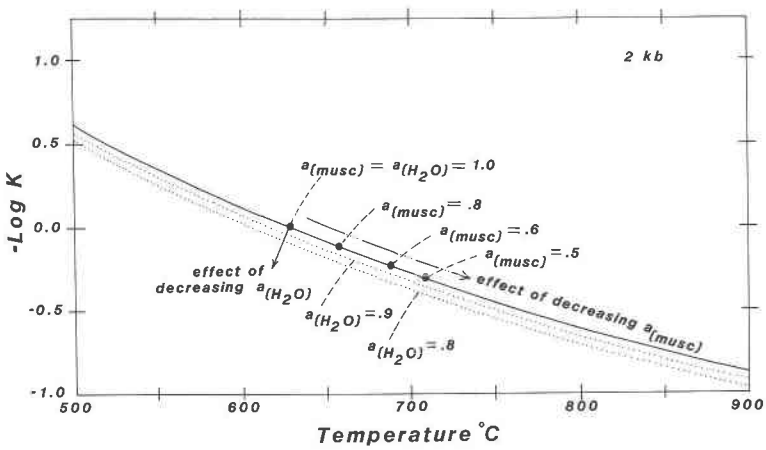

Fig. 5. The reaction $KAl_2(AlSi_3O_{10})(OH)_2$ (muscovite) + SiO_2 (quartz) = $KAlSi_3O_3$ (maximum microcline) + Al_2SiO_5 (sillimanite) + H_2O (liq.) plotted as a function of $-\log K$ of the reaction and temperature, at 2 kbar. All phases involved in the reaction are stable at unit activity at the point where $-\log K = 0$. Decreasing $-\log K$ from 0 along the solid curve illustrates the effective increased thermal stability limit of the assemblage muscovite + quartz + maximum microcline + sillimanite + H_2O when activities of all phases except for muscovite are held constant at 1, such that $-\log K = \log a_{\text{muscovite}}$. The dotted curves illustrate the effective decrease of the thermal stability limit of the assemblage as a_{H_2O} decreases from 1.

An approximation of the activity of nonpocket muscovite was calculated from the average of 10 microprobe analyses of muscovite sampled from the pegmatite zone (Table 10). This calculation was computed for the thermodynamic component $KAl_2(AlSi_3)O_{10}(OH)_2$ in solid solution with $NaAl_2(AlSi_3)O_{10}(OH)_2$, where the standard-state thermodynamic data for these components are given by Helgeson et al. (1978) and refer to a completely ordered tetrahedral-site distribution of Al^{3+} and Si^{4+}, discussed by Bird and Norton (1981). The corresponding activity-composition relation for the pure muscovite component, given by Bird and Norton (1981), is

$$a = (X_{K^+,A})(X_{Al^{3+},M2})^2(X_{Al^{3+},T1O})(X_{Si^{4+},T1m})(X_{Si^{4+},T2})^2(X_{OH^-})^2.$$

This relation was derived from Equations 46 through 48 of Helgeson et al. (1978) and equations and data reported by Helgeson and Aagaard (1985) and agrees with ordered standard-state site distributions, equations, and data given by Helgeson et al. (1978) for muscovite.

The analyses of nonpocket muscovite from the pegmatite zone yield an average composition of $(K_{0.86}Na_{0.14})$-$(Al_{0.96}Fe_{0.03}Ti_{<0.01}Mn_{<0.01})_2(Al_{0.96}Si_{3.04})O_{10}(OH_{0.885}F_{0.10})_2$. Applying this composition to the above activity-composition relation allows an approximate calculation for activity of the pure muscovite component to be made based primarily on K, Al, and OH distribution:

$$a \approx (X_{K^+,A})(X_{Al^{3+},M2})^2(X_{Al^{3+},T1O})(X_{OH^-})^2 \approx 0.6$$

which shifts the upper thermal stability limit of the assemblage microcline + muscovite + quartz + H_2O to 690°C. This approximate value of $a_{\text{muscovite}} = 0.6$ supports modeling the evolution of the Little Three system with nonstoichiometric muscovite to account for the common occurrence of the assemblage muscovite + K-feldspar + quartz observed throughout most zones of the pegmatite-aplite dike.

Deviation from unit activity of H_2O in the coexisting fluid phase, however, would promote the reverse effect of decreasing muscovite activity. These opposite effects are illustrated in Figure 5, which graphs the reaction

muscovite + quartz = sillimanite + microcline + H_2O

at 2-kbar pressure, as a function of temperature and $-\log K$ of the reaction. Figure 5 shows that where $-\log K = 0$, activity of all phases is unity, and the corresponding temperature of 630°C represents the upper thermal stability limit where all stoichiometric phases are stable together. Following the solid curve in Figure 5 to increasing temperatures illustrates the effective expansion of the muscovite stability field resulting from depressing muscovite activity, if the activities of all other phases are held constant at unity such that $-\log K = \log a_{\text{muscovite}}$. The dotted curves project the reaction with decreased activity of water from unity down through 0.8, illustrating how decreased activity of H_2O in the fluid phase serves to depress the upper thermal stability limit of the mineral assemblage muscovite + quartz + microcline.

The effects of depressing a_{H_2O} in the fluid phase of the Little Three system, however, is presumed to be negligible. Fluid-inclusion data reported by Taylor et al. (1979) from Little Three pocket material yield extremely low X_{CO_2} values (~0.001), and data from neighboring district pocket material yield average equivalent NaCl salinities of 4 to 5 wt% (<1 molal). The effects of such low salinities on the activity of H_2O are shown by Helgeson (1981, Fig. 7.31) to be extremely low; at 2 kbar, over the temperature range 0–500°C, a 1 molal NaCl solution is shown to depress H_2O activity from unity to approximately 0.98. This decrease from unit activity is insignificant on the loga-

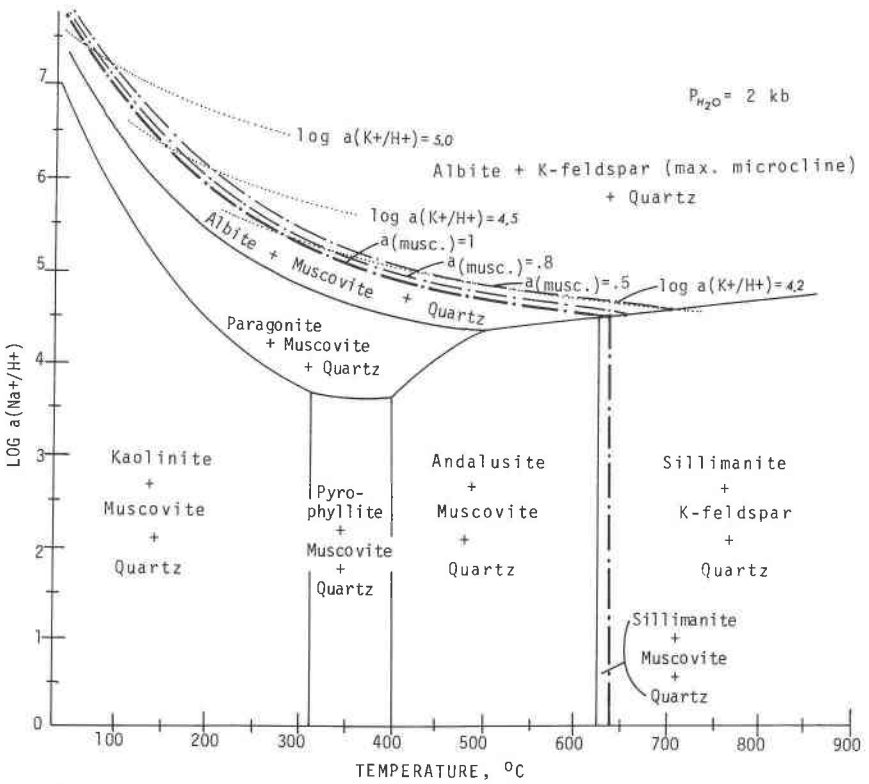

Fig. 6. Phase relations for the system Na_2O-K_2O-Al_2O_3-H_2O plotted as a function of log $a_{(Na^+/H^+)}$ and temperature, for pegmatite-aplite mineral assemblages at quartz saturation, in equilibrium with a supercritical fluid phase. $P_T = P_{H_2O}$ = 2 kbar; a_{H_2O} = 1. Solid lines denote stability field boundaries calculated for stoichiometric minerals. Dot-dashed lines project the K-feldspar–muscovite boundary, contoured for decreasing $a_{muscovite}$. Stippled lines contour log $a_{(K^+/H^+)}$ of the fluid phase.

rithmic scale and therefore is not considered an important factor in the phase-relation calculations here.

To trace the path along which muscovite + K-feldspar + albite + quartz + aqueous solution all coexist requires evaluation of the equation

$$NaAlSi_3O_8 + 2KAlSi_3O_8 + 2H^+ = KAl_2(AlSi_3O_{10})(OH)_2 + K^+ + Na^+ + 6SiO_2$$

that simultaneously relates all four solid phases as well as the electrolytes of interest. The corresponding mass-action equation is

$$\log K = \log a_{(K^+/H^+)} + \log a_{Na^+/H^+)} + \log[(a^6_{quartz})\,(a_{muscovite})/(a^2_{K\text{-}feldspar})\,(a_{albite})],$$

which can be solved for either log $a_{(K^+/H^+)}$ or log $a_{(Na^+/H^+)}$ in terms of the other. With the use of this mass-action equation, combined with the known log $a_{(K^+/H^+)}$ values at a given temperature for the K-feldspar–muscovite reaction boundary from the K_2O-Al_2O_3-SiO_2-H_2O system, contours of log $a_{(K^+/H^+)}$ and the K-feldspar + muscovite reaction line were projected onto the albite field of Figure 6. Dashed lines also trace the K-feldspar + muscovite + albite + quartz path with muscovite activity reduced from unity to 0.8 and 0.5. As crystallization progresses with falling temperatures, log $a_{(K^+/H^+)}$ of the fluid phase is predicted to remain essentially constant within the range of 4.10 (cf. Fig. 4a), while log $a_{(Na^+/H^+)}$ rises gradually several tenths of a log unit from approximately 4.55 to 4.75. The exact values at any given temperature, however, are dependent on deviation from mineral stoichiometry or unit activity of H_2O.

Figure 7 plots isobaric isothermal activity diagrams adding H^+ and F^- to the system K_2O-Al_2O_3-SiO_2-H_2O, at probable primary pocket-forming temperatures for F-bearing pockets containing topaz. These figures show the systematic increase of log $a_{(H^+)(F^-)}$ and nearly constant log $a_{(K^+/H^+)}$ of the fluid phase, with decreasing temperatures, necessary to stabilize the pocket assemblage K-feldspar + quartz + OH-muscovite + F-topaz + H_2O.

Summary and Conclusions

Field relations coupled with experimental and isotopic data from the literature support crystallization of the Little Three pocket pegmatite–aplite dike from a magmatic system involving an initially hydrous aluminosilicate melt with coexisting supercritical aqueous fluid. Closed-system fractional crystallization of the basal aplite largely from the melt presumably began shortly after emplacement of the dike at approximately 730–700°C, with subsequent crystallization of the associated graphic pegmatite hanging wall from water-saturated melt in the presence of a su-

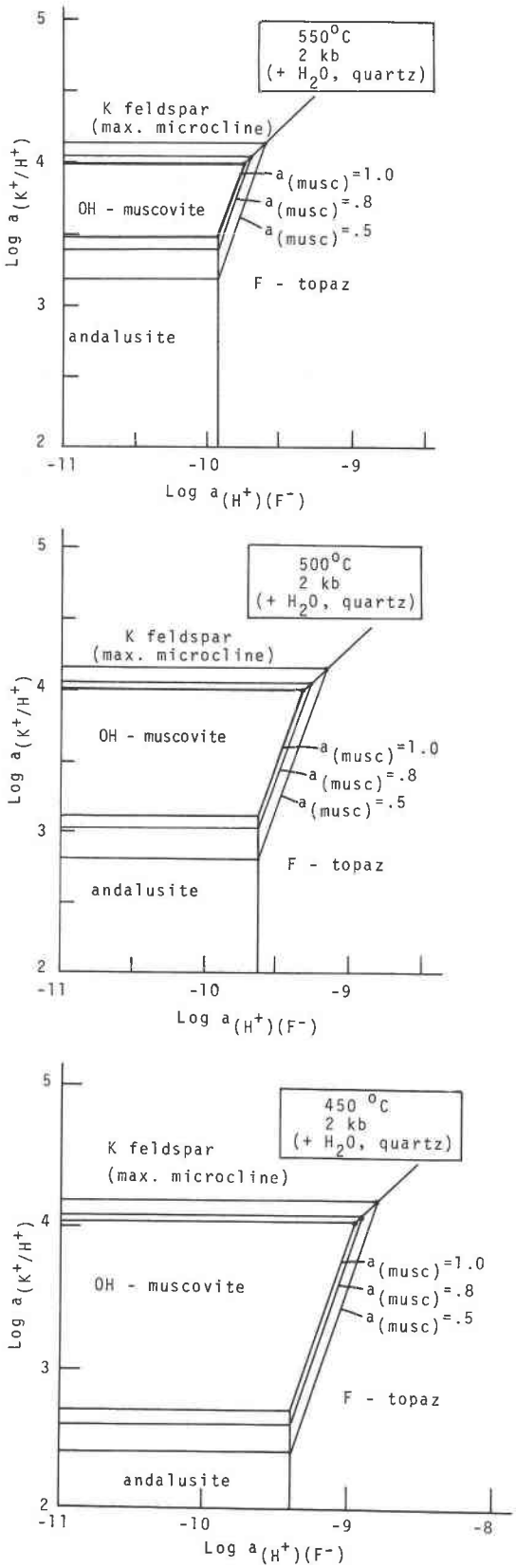

percritical aqueous phase. Pocket pegmatite evidently formed last, in the near-absence of silicate melt, at temperatures of approximately 565–525°C. Crystallization of the large pockets may have persisted to even lower temperatures, where unusually high concentrations of F, B, and Li are believed to have strongly affected the behavior of the melt and vapor phase.

Electron-microprobe analyses of minerals from the New Spaulding pocket yield a pocket assemblage that includes elbaite with an uncommonly high Mn content; lepidolite with nearly complete replacement of F or OH; moderately F-rich topaz; quartz; and nearly pure alkali feldspars including maximum microcline (Or_{98}) perthite megacrysts and low albite (Ab_{99}) occurring as cleavelandite. Minor phases found in pockets from the Little Three main dike include microlite-uranmicrolite, stibio-bismuto-columbite-tantalite, and columbite, plus very rare beryl, apatite, and hambergite. X-ray analyses of samples from other zones of the pegmatite-aplite dike indicate that the perthite composition of the graphic hanging wall is a maximum microcline host with exsolved low albite lamellae. Elongate perthite crystals sampled from the central quartz-perthite-albite pegmatite zone, however, yield an intermediate microcline structure and commonly show an abrupt light- to dark-colored transition adjacent to the pocket zone; the dark-colored material was determined by X-ray diffraction methods to be orthoclase. No pocket orthoclase was recovered from the Little Three main dike, although one specimen from a pegmatite exposure adjacent to the Little Three main dike was found.

Large pockets such as the New Spaulding pocket show extensive mineral segregation with alkali partitioning partially or markedly reversed relative to that observed throughout the bulk of the system. Minerals from the New Spaulding pocket are distributed such that the K-bearing minerals including lepidolite and microcline are largely distributed floorward, whereas the Na-, B-, and Si-rich minerals incuding cleavelandite, elbaite, and quartz tend to form along the ceiling. Fluorine-bearing phases were distributed ubiquitously, although the F-rich lepidolite along the floor yields proportionately the highest fluorine replacement of the hydroxyl site of all hydrous phases present in the pockets. Al and Si were also ubiquitous, although large quartz crystals were more commonly found projecting down from the roof, and abundant topaz was found intergrown along the floor, but not obviously at-

←

Fig. 7. Phase relations for the system K_2O-Al_2O_3-H_2O-HF plotted as a function of log $a_{(K^+/H^+)}$ and log $a_{(H^+)(F^-)}$, at 2-kbar pressure, at probable crystallization temperatures for high F-bearing pockets. These relations illustrate the systematic increase of $a_{(H^+)(F^-)}$ in the fluid phase, with decreasing temperatures, necessary to stabilize the assemblage maximum microcline + muscovite + quartz + fluor-topaz. Solid lines denote stability field boundaries calculated for unit activity of H_2O and unit activity of all minerals except muscovite; pocket muscovite is modeled by contouring $a_{muscovite}$ from 1 down through 0.5.

tached. Experimental data reported on high F and B concentrations in the system $KAlSi_3O_8$-$NaAlSi_3O_8$-SiO_2-H_2O show that these volatile constituents may serve to modify the behavior of alkalis in a similar manner to that observed in the New Spaulding pocket, to lower the liquidus temperature of the residual silicate melt, to promote crystal growth from the vapor phase, and to increase the silica solute capability of the vapor phase.

Predictions from calculations of equilibrium phase relations among stoichiometric minerals in the system Na_2O-K_2O-Al_2O_3-SiO_2-H_2O are not entirely consistent with the observed mineral assemblages at the Little Three mine; however, the approximation of mineral stoichiometry is useful as a basis for predicting general trends among aqueous-electrolyte ratios, effected by changing temperature and mineral assemblages. Solution-mineral-equilibria calculations for stable phases in the system K_2O-Na_2O-Al_2O_3-SiO_2-H_2O are particularly useful for modeling the nonpocket portions of the pegmatite-aplite system, where the bulk composition lies near the thermal minimum of the haplogranite system. This graphical approach indicates the virtual temperature independence of log $a_{(K^+/H^+)}$ and log $a_{(Na^+/H^+)}$ given the stable assemblage K-feldspar + albite + quartz + muscovite. Microprobe analyses of pocket phases suggest that while alkali feldspar compositions are virtually pure end members with minor impurities, the mica structures may host major substitutions. Modeling muscovite nonstoichiometry by decreasing the activity of the pure component from unity down to 0.5 significantly increases the thermal stability limit of the assemblage K-feldspar + albite + quartz + muscovite at 2 kbar from 625°C upward to 700°C. Substitutions into the muscovite structure may, therefore, help to stabilize this assemblage at the outer zones of the dike, where initial temperatures of formation are expected to have been approximately 700°C.

Acknowledgments

We wish to thank J. Consul of the Analytical Branch, U.S. Geological Survey, Menlo Park, California, for determination of B and Li contents of tourmaline samples; N. Conklin of the Branch of Analytical Laboratories, U.S. Geological Survey, Denver, Colorado, for emission spectrographic analyses; E. Winterburn and M. Hochella of Stanford University for their help with X-ray diffraction analyses and cell-dimension determinations. We also wish to thank G. Lumpkin, P. Modreski, and P. Černý for reviewing an earlier version of the manuscript and acknowledge the help of B. Mills, G. Holzhausen, and P. Long during the initial excavation of the New Spaulding pocket.

Partial funding for this project was provided by NSF grants EAR 80-16911 (G.E.B.) and DMR 80-20248-A4 (G.E.B.), and by the Fink graduate award (L.A.S.) through the Stanford Geology Department.

References

Bailey, J.C. (1977) Fluorine in granitic rock and melts: A review. Chemical Geology, 19, 1–42.

Bailey, S.W. (1980) Structure of layer silicates. Chapter 1. In Crystal structures of clay minerals and their X-ray identification. Mineralogical Society, London. Monograph 5, 1–123.

Barton, M.D., Haselton, H.T., Hemingway, B.S., Kleppa, O.J., and Robie, R.A. (1982) The thermodynamic properties of fluor topaz. American Mineralogist, 67, 350–355.

Bence, A.E., and Albee, A.L. (1968) Empirical correction factors for the electron microanalysis of silicates and oxides. Journal of Geology, 76, 382–403.

Bird, D.K., and Norton, D.L. (1981) Theoretical predictions of phase relations among aqueous solutions and minerals: Salton Sea geothermal system. Geochimica et Cosmochimica Acta, 45, 1479–1493.

Borg, I.Y., and Smith, D.K. (1969) Calculated X-ray powder patterns for silicate minerals. Geological Society of America Memoir 122.

Burnham, C.W., and Jahns, R.H. (1962) A method for determining the solubility of water in silicate melts. American Journal of Science, 260, 721–745.

Chorlton, L.B., and Martin, R.F. (1978) The effect of boron on the granite solidus. Canadian Mineralogist, 16, 239–244.

Colby, J.W. (1968) Quantitative analysis of thin insulating films. In J. Newkirk, G. Mallett, and H. Pfeiffer, Eds. Advances in X-ray analysis, Volume 11. Plenum Press, New York.

Dietrich, R.V. (1985) The tourmaline group. Van Nostrand–Rinehold Co., New York.

Dingwell, D.B., Scarfe, C.M., and Cronin, D.J. (1985) The effect of fluorine on viscosities in the system Na_2O-Al_2O_3-SiO_2; implications for phonolites, trachytes, and rhyolites. American Mineralogist, 70, 80–87.

Donnay, J.D.H., and Harker, D. (1937) A new law of crystal morphology extending the law of Bravais. American Mineralogist, 22, 446–467.

Fenn, P.M. (1986) On the origin of graphic granite. American Mineralogist, 71, 325–330.

Foord, E.E. (1976) Mineralogy and petrogenesis of layered pegmatite-aplite dikes in the Mesa Grande district, San Diego County, California. Ph.D. dissertation, Stanford University, Stanford, California.

——— (1977) The Himalaya dike system, Mesa Grande district, San Diego County, California. Mineralogical Record, 8, 461–474.

——— (1982a) Bismuthian stibiocolumbite-tantalite and other minerals from the Little Three mine, Ramona, California. Fourth annual MSA-FM Symposium, February 1981, Tucson, Arizona. In G.E. Brown, Jr., Ed. The mineralogy of pegmatites. American Mineralogist, 67, 181–182.

——— (1982b) Minerals of tin, titanium, niobium, and tantalum in granitic pegmatites. In P. Černý, Ed. Granitic pegmatites in science and industry, 187–238. Mineralogical Association of Canada Short Course Handbook 8.

Foord, E.E., Martin, R.F., and Long, P.E. (1979) Potassic feldspars from pocket pegmatites, San Diego County, California. Geological Society of America Abstracts with Programs, 11, 427.

Foord, E.E., Starkey, H.C., and Taggart, J.E., Jr. (1986) Mineralogy and paragenesis of "pocket clays" and associated minerals in complex granitic pegmatites, San Diego County, California. American Mineralogist, 71, 428–439.

Hawthorne, F.C., and Černý, P. (1982) The mica group. In Černý, Ed. Granitic pegmatites in science and industry, 99–133. Mineralogical Association of Canada Short Course Handbook 8.

Helgeson, H.C. (1981) Prediction of the thermodynamic properties of electrolytes at high pressures and temperatures. In F. Wickman and D. Rickard, Eds. Chemistry and geochemistry of solutions at high temperatures and pressures. Physics and Chemistry of the Earth, 13 and 14, 133–175. Pergammon Press, New York.

Helgeson, H.C., and Aagaard, Per. (1985) Activity/composition relations among silicates and aqueous solutions. I. Thermodynamics of intrasite mixing and substantial order/disorder in minerals. American Journal of Science, 285, 769–844.

Helgeson, H.C., and Kirkham, D.H. (1974) Theoretical prediction of the thermodynamic behavior of aqueous electrolytes at

high pressures and temperatures: I. Summary of the thermodynamic/elestrostatic properties of the solvent. American Journal of Science, 274, 1089–1198.

——— (1976) Theoretical prediction of the thermodynamic behavior of aqueous electrolytes at high pressures and temperatures: III. Equation of state for aqueous species at infinite dilution. American Journal of Science, 276, 97–240.

Helgeson, H.C., Delaney, J.M., Nesbitt, H.W., and Bird, D.K. (1978) Summary and critique of the thermodynamic properties of rock-forming minerals. American Journal of Science, 278-A, 1–229.

Helgeson, H.C., Kirkham, D.H., and Flowers, G.C. (1981) Theoretical prediction of the thermodynamic behavior of aqueous electolytes at high pressures and temperatures: IV. Calculation of activity and osmotic coefficients and apparent molal and standard and relative partial molal properties to 600°C and 5 kb. American Journal of Science, 281, 1249–1493.

Hovis, G.L. (1974) A solution calorimetric and X-ray investigation of Al/Si distribution in monoclinic potassium feldspars. In W.S. MacKenzie and J. Zussman, Eds. The feldspars. 114–144. Crane, Russak, and Co., New York.

Jahns, R.H. (1955) The study of pegmatites. Economic Geology, 50th Anniversary Volume, 1023–1130.

——— (1982) Internal evolution of pegmatite bodies. In P. Černý, Ed. Granitic pegmatites in science and industry, 293–327. Mineralogical Association of Canada Short Course Handbook 8.

Jahns, R.H., and Burnham, C.W. (1969) Experimental studies of pegmatite genesis: I. A model for the derivation and crystallization of granitic pegmatites. Economic Geology, 64, 843–864.

Jahns, R.H., and Tuttle, O.F. (1963) Layered pegmatite-aplite intrusives. Mineralogical Society of America Special Paper 1, 78–92.

Jahns, R.H., and Wright, L.A. (1951) Gem- and lithium-bearing pegmatites of the Pala district, San Diego County, California. California Division of Mines and Geology Special Report 7-A.

Kunitz, W. (1929) Die Mischungsreihen in der Turmalingruppe und die Genetischen Beziehungen zwischen Turmalinen und Glimmern. Chemie der Erde, 4, 208–251.

London, D. (1986a) The magmatic-hydrothermal transition in the Tanco rare-element pegmatite: evidence from fluid inclusions and phase equilibrium experiments. American Mineralogist, 71, 376–395.

——— (1986b) Formation of tourmaline-rich gem pockets in miarolitic pegmatites. American Mineralogist, 71, 396–405.

London, D., and Burt, D.M. (1982) Lithium minerals in pegmatites. In P. Černý, Ed. Granitic pegmatites in science and industry, 63–98. Mineralogical Association of Canada Short Course Handbook 8.

Manning, D.A.C. (1981) The effect of fluorine on liquidus phase relationships in the system Qz-Ab-Or with excess water at 1 kb. Contributions to Mineralogy and Petrology, 76, 206–215.

Martin, R.F. (1982) Quartz and the feldspars. In P. Černý, Ed. Granitic pegmatites in science and industry, 41–62. Mineralogical Association of Canada Short Course Handbook 8.

Mckenzie, W.F. (1980) Estimation of the dielectric constant of water and the thermodynamic properties of aqueous species to 900°C at 2 kb. Ph.D. dissertation, University of California, Berkeley.

Mckenzie, W.F., and Helgeson, H.C. (1984) Calculated phase relations among silicates, copper iron sulfides, and aqueous solutions at magmatic temperatures. Geological Society of America Abstracts with Programs, 12, 481.

McTigue, J.W. (1981) Chemical interaction of aqueous solutions with an alkali-feldspar–muscovite–quartz assemblage in a crystallizing pegmatite: Sprue Pine district, North Carolina. M.S. thesis, University of Arizona, Tucson.

Munoz, J.L. (1971) Hydrothermal stability relations of synthetic lepidolite. American Mineralogist, 56, 2069–2087.

Pichavant, M. (1981) An experimental study of the effect of boron on a water-saturated haplogranite at 1 kbar vapour pressure. Geological applications. Contributions to Mineralogy and Petrology, 76, 430–439.

——— (1983) Melt-fluid interaction deduced from studies of silicate-B_2O_3-H_2O. Bulletin de Minéralogie, 106, 201–211.

Schmetzer, K., and Bank, H. (1984) Crystal chemistry of tsilaisite (manganese tourmaline) from Zambia. Neues Jahrbuch fuer Mineralogie. Monatshefte, 2, 61–69.

Shigley, J.E. (1982) Phosphate minerals in granitic pegmatites. Ph.D. dissertation, Stanford University, Stanford, California.

Shigley, J.E., and Brown, G.E., Jr. (1985) Occurrence and alteration of phosphate minerals at the Stewart Pegmatite, Pala District, San Diego County, California. American Mineralogist, 70, 395–408.

Simpson, D.R. (1962) Graphic granite from the Ramonna pegmatite district, California. American Mineralogist, 47, 1123–1138.

——— (1965) Geology of the central part of the Ramona pegmatite district, San Diego County, California. California Division of Mines and Geology Special Report 86, 3–23.

Slivko, M.M. (1959) On manganese tourmalines. Mineralogichesky Sbornik, Lvovskogo Geologicheskogo Obshchestva, 13, 139–148 (transl. International Geological Review, 3, 195–201.)

Stewart, D.B. (1963) Petrogenesis and mineral assemblages of lithium-rich pegmatites. (abs.) Geological Society of America Special Paper 16, 159.

——— (1978) Petrogenesis of lithium-rich pegmatites. American Mineralogist, 63, 970–980.

Stewart, D.B., and Wright, T. (1974) Al/Si order and symmetry of natural alkali feldspars and the relationship of strained cell parameters to bulk composition. Bulletin de la Société Française de Minéralogie et de Cristallographie, 97, 356–377.

Taylor, B.E., Foord, E.E., and Friedrichsen, H. (1979) Stable isotope and fluid inclusion studies of gem-bearing granitic pegmatite-aplite dikes, San Diego County, California. Contributions to Mineralogy and Petrology, 68, 187–205.

Thompson, J.B., Waldbaum, D.R., and Hovis, G.L. (1974) Thermodynamic properties related to ordering in endmember alkali feldspars. In W.S. MacKenzie and J. Zussman, Eds. The feldspars, 218–248. Crane, Russak, and Co., New York.

Tuttle, O.F., and Bowen, N.L. (1958) Origin of granite in the light of experimental studies in the system $NaAlSi_3O_8$-$KAlSi_3O_8$-SiO_2-H_2O. Geological Society of America Memoir 74.

Walther, J.V., and Helgeson, H.C. (1977) Calculation of the thermodynamic properties of aqueous silica and the solubility of quartz and its polymorphs at high pressures and temperatures. American Journal of Science, 277, 1315–1351.

Wyllie, P.J., and Tuttle, O.F. (1961) Experimental investigation of silicate systems containing two volatile components: Part II. The effects of NH_3 and HF, in addition to H_2O, on the melting temperatures of albite and granite. American Journal of Science, 259, 128–143.

——— (1964) Experimental investigation of silicate systems containing two volatite components: Part III. The effects of SO_3, P_2O_5, HCl, and Li_2O, in addition to H_2O, on the melting temperatures of albite and granite. American Journal of Science, 262, 930–939.

Manuscript received May 24, 1985
Manuscript accepted November 23, 1985